The Astrophysical Journal, 644:1118–1144, 2006 June 20

NONTHERMAL HIGH-ENERGY EMISSION FROM COLLIDING WINDS OF MASSIVE STARS

A. Reimer,[1,2] M. Pohl,[3] and O. Reimer[1]

Received 2005 October 24; accepted 2006 February 20

ABSTRACT

Colliding winds of massive star binary systems are considered as potential sites of nonthermal high-energy photon production. Motivated by the detection of synchrotron radio emission from the colliding wind location, we here investigate the properties of high-energy photon production in colliding winds of long-period WR+OB systems. Analytical formulae for the steady state proton- and electron-particle spectra are derived assuming diffusive particle acceleration out of a pool of thermal wind particles, taking into account adiabatic and all relevant radiative losses, and include advection/convection out of the wind collision zone. This includes analytical approximations for the electron energy losses in the Klein-Nishina transition regime. For the first time in the context of CWB systems, our calculations use the full Klein-Nishina cross section and account for the anisotropy of the inverse Compton scattering process. This leads to orbital flux variations by up to several orders of magnitude, which may, however, be blurred by the system's geometry. Both anisotropy and Klein-Nishina effects may yield characteristic spectral and variability signatures in the γ-ray domain. Since propagation effects lead to a deficit of low-energy particles in the convection-dominated zone, one expects imprints in the radiation spectra. If protons are accelerated to at least several GeV, π^0-decay γ-rays might be observable, depending on the injected electron-to-proton ratio. We show that photon-photon pair production is generally not negligible, potentially affecting the emitted spectrum above $\sim$50 GeV, depending on orbital phase and system inclination. The calculations are applied to the archetypal WR+OB systems WR 140 and WR 147 to predict their expected spectral and temporal characteristics and to assess their detectability with current and upcoming γ-ray experiments.

Subject headings: binaries: general — gamma rays: theory — radiation mechanisms: nonthermal — stars: early-type — stars: winds, outflows

Online material: color figures

1. INTRODUCTION

Early-type stars (O, early B, Wolf-Rayet [WR] stars) are hot stars ($T_{\rm eff} > 10{,}000$ K) with masses $>20\,M_\odot$. They are known to possess some of the strongest sustained winds among Galactic objects. As a class WR stars have the highest known mass loss $\dot{M} \sim 10^{-4}$ to $10^{-5}\,M_\odot\ {\rm yr}^{-1}$ of any stellar type. The supersonic winds of massive stars may reach terminal velocities of $v_\infty > 1000$–$5000\ {\rm km\ s}^{-1}$ (Cassinelli 1979); their kinetic energies $L_w = \dot{M} v_\infty^2/2$ but rarely exceed 1% of the bolometric radiative energy output of typically $\sim 10^{38}$ ergs s^{-1}.

In recent years massive stars have been connected to several high-energy phenomena: they are suspected to be the progenitor of some types of γ-ray bursts (Woosley 1993; Paczynski 1998) and are known to be an interacting medium for the blast wave expelled from supernova explosions. Triggered by the detections of several γ-ray sources by the Energetic Gamma-Ray Experiment Telescope (EGRET) that are still left unidentified but found in positional coincidence with massive binary systems (Kaul & Mitra 1997; Romero et al. 1999), and motivated by the detection of synchrotron radiation from the collision region in some massive binaries, these systems have also been proposed as potential sites of nonthermal high-energy photon production (Montmerle 1979; Eichler & Usov 1993; Romero et al. 1999).

Binary systems containing a massive star and a compact companion are also proposed sites of γ-ray production (Tavani & Arons 1997; Kirk et al. 1999). One of these, PSR 1259−63, has recently been detected to emit TeV photons (Aharonian et al. 2005a) when the pulsar wind beam passes the accretion disk of the compact object. Although the operating radiation processes in pulsar wind binaries may be similar to colliding wind systems, the different nature and geometry of the soft photon field and the winds will cause a distinguishably different spatial and temporal behavior of the emitted radiation.

Unlike in a wind of a single massive star in which particles have been proposed to be accelerated by either multiple weak shocks from line-driven instabilities (Lucy & White 1980; White 1985) to compensate for the expansion and radiative losses even close to the stellar photosphere, or at the terminal shocks created by the interaction with the swept-up interstellar medium (Cassé & Paul 1980; Völk & Forman 1982), the collision of supersonic winds produces strong shocks where both electrons and protons can be efficiently accelerated to high energies through first-order Fermi acceleration (Eichler & Usov 1993).

In this latter scenario the shock region is exposed to both, a strong radiation field in the ultraviolet (UV) range from the participating hot stars, and their magnetic fields. The detection of synchrotron radiation from such collision regions, implied by the flat or negative spectral indices and brightness temperatures of 10^6–10^7 K, proves the existence of magnetic fields, as well as relativistic electrons in the collision region of some massive binary systems (Abbott et al. 1986). In addition, observations of radio emission reveal an extended region of synchrotron radiation (Dougherty et al. 2000). In some binaries (e.g., WR 147, WR 146, OB2 No. 5) the collision region between the main-sequence stars has been resolved in the radio band showing an extended, slightly elongated nonthermal feature on Very Large Array (VLA) and MERLIN images (Dougherty et al. 1996,

[1] W. W. Hansen Experimental Physics Laboratory, Stanford University, 445 Via Palou Mall, Stanford, CA 94305; afr@stanford.edu, olr@stanford.edu.

[2] Institut für Theoretische Physik, Lehrstuhl IV: Weltraum- und Astrophysik, Ruhr-Universität Bochum, D-44780 Bochum, Germany; afm@tp4.rub.de.

[3] Department of Physics and Astronomy, Iowa State University, Ames, IA 50011; mkp@iastate.edu.

2000; Contreras et al. 1997) in addition to the free-free emission from the spherical wind of the stars. Recently, the extended wind-wind collision region from WR 147 has been detected in the X-ray band by *Chandra* (Pittard et al. 2002). Early models to explain nonthermal radio emission from CWB systems (e.g., Eichler & Usov 1993) have recently been substantiated by including hydrodynamic simulations (e.g., Dougherty et al. 2003; Pittard et al. 2006).

Those electrons with energy $\gamma_e m_e c^2$ will inevitably also be responsible for a nonthermal high-energy component at $\sim\gamma_e^2\epsilon_T$ produced through inverse Compton (IC) scattering of the dense stellar radiation field with characteristic energy ϵ_T. Interestingly, recent *XMM* and simultaneous VLA observations of the WR star 9 Sgr might already hint at a nonthermal X-ray component. While the hard X-ray component of 9 Sgr could be equally well fitted by either a hot multitemperature thermal model with $kT \geq 1.5$ keV or a steep power law with power-law index $\geq$2.9, suggesting a compression ratio $\leq$1.8, the VLA spectrum at the time of the *XMM* observations was clearly nonthermal, thus indicating a similar compression ratio of $\sim$1.7 (Rauw et al. 2002).

The relativistic electrons will also lose some fraction of their energy due to nonthermal bremsstrahlung in the field of ions that are embedded in the stellar winds. It has been estimated, however, that the resulting nonthermal bremsstrahlung component in the γ-ray domain at $\sim(\gamma_e/2)m_e c^2$ from electrons of energy $\gamma_e m_e c^2$ will be a minor contribution to the overall emission because of the ambient gas densities involved (Benaglia & Romero 2003).

If electron acceleration is also accompanied with acceleration of protons out of the thermal pool of wind material, then proton interactions with the ambient ions will produce γ-rays through the hadronic neutral pion decay channel $p + p \longrightarrow \pi^0 + X$, $\pi^0 \longrightarrow \gamma + \gamma$. In addition, radiation from the secondary pairs, generated through the decay of charged mesons that are produced by the hadronic *pp*-collisions, is also expected to contribute to the overall broadband spectrum. The π^0-decay radiative channel has already been considered in the past in the context of winds from massive stars (Chen & White 1991; White & Chen 1992; White 1985, for the case of single O stars); however, neither propagation effects inside the extended collision region nor competing loss mechanisms (such as expansion losses in the wind) have been taken into account.

The goal of this work is to extend the model of nonthermal emission in the high-energy domain from the colliding wind region in massive star binary systems to include all relevant energy losses and simultaneously consider the propagation effects that affect a relativistic particle distribution in such an environment. After a brief description of the geometry considered in this work (§ 2), we evaluate the evolution of both proton and primary electron spectra on the basis of a simplified diffusion loss equation. In § 3 we calculate the expected photon emission due to the IC process (for the first time including Klein-Nishina and anisotropy effects), relativistic bremsstrahlung, and the γ-rays from the decay of π^0 that are produced in hadronic proton-proton collisions. The total expected γ-ray spectrum is corrected for photon absorption in the UV radiation field of the massive stars. We apply our model to the well-known long-period binary system WR 140 and the already mentioned WR 147 in § 4. Our conclusions summarize our results and provide an outlook on the detectability of CWB systems with upcoming instruments like *Gamma-Ray Large Area Space Telescope* (*GLAST*), and the current generation of imaging atmospheric Cerenkov telescopes (IACTs).

2. THE GEOMETRIC MODEL OF A COLLIDING WIND REGION

The typical radial velocity profile $V(x)$ of winds from hot massive stars obeys the relation

$$V(x) = v_\infty \left(1 - \frac{r_s}{x}\right)^\beta$$

(Lamers & Casinelli 1999), with $\beta \simeq 0.8$, r_s the radius of the star, and v_∞ the terminal velocity. Recent observations indicate the existence of clumping in the wind (e.g., Moffat 1996; Schild et al. 2004). For our schematic picture here we shall postpone the effects of clumping to later work and consider a homogeneous uniform wind. We also neglect any small-scale shocks within the wind. The winds from binary systems flow nearly radially until they collide to form a discontinuity at the location of ram pressure balance, and forward and reverse shocks. In the shock region the gas is heated to temperatures of 10^6–10^8 K (Luo et al. 1990; Stevens et al. 1992; Usov 1992), which causes strong thermal X-ray emission. Behind the shock the gas expands sideways from the wind collision region along the contact surface out to larger r. We therefore distinguish two regions of the extended emission site (see Fig. 1): In the acceleration zone $r \leq r_0$ (first-order) diffusive acceleration provides high-energy particles out of a thermal pool. While the stellar winds prohibit the escape of energetic particles on the upstream side of the shocks, we anticipate that in the downstream region spatial diffusion is more efficient than convective/advective motion (which we call "convection" in the following) in transporting particles to the boundary of the acceleration zone at $r = r_0$. Subsequent to their diffusive escape from the acceleration zone, the energetic particles enter the convection-dominated zone $r > r_0$. The characteristic radius $r = r_0$ is defined by equality of the convection timescale $t_{\rm conv}$ and the diffusion timescale $t_{\rm diff}$.

Furthermore, we demand that the distance of the emission region from the low-momentum wind source is large compared to the longitudinal extension of the emission region. While in reality the form of the contact surface is bent toward the star that shows the lower wind momentum, which is observed as arcs of emission on radio images (e.g., Dougherty et al. 2005), we consider here the simplified geometry of a cylinder disk (see Fig. 1). This may be justified by the rapid particle energy loss rates that do not allow the transport of energetic particles to large distances from their acceleration site. In other words, most particle energy losses are expected to appear close to the acceleration zone, where a cylindrical geometry appears a reasonable approximation. The thickness d of the cylinder-like emission region is governed by the velocity of the hitting winds. We further neglect here the interaction of the stellar radiation fields on the wind structure (Gayley et al. 1997; Stevens & Pollock 1994), which is justified for long-period binaries.

In the case of a collision between the spherical wind of a primary (e.g., a WR star) and a secondary companion (e.g., an OB star) that have reached their terminal velocities ($v_{\rm OB}$, $v_{\rm WR}$), the location of the shock is determined by the balance of the ram pressure of both winds,

$$\rho_{\rm OB} v_{\rm OB}^2 = \rho_{\rm WR} v_{\rm WR}^2, \qquad (1)$$

where $\rho_{\rm OB}$, $\rho_{\rm WR}$ are the densities of the gas ahead of and near the shock of the stellar winds of the OB and WR stars, respectively.

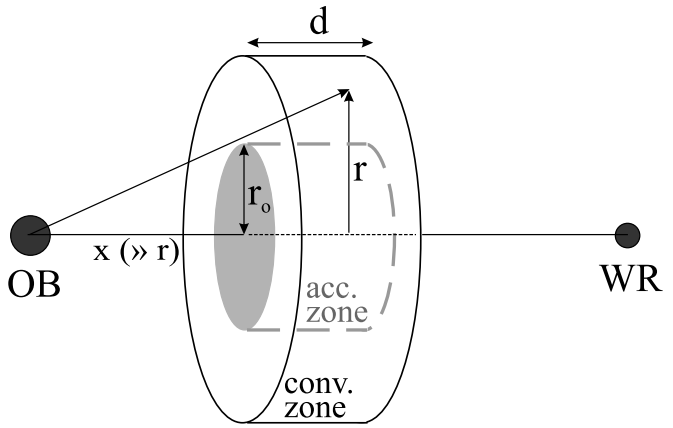

FIG. 1.—Model geometry for the collision of two stellar winds of a WR+OB binary system. A strong shock is created in the wind collision region, which is situated at a distance $x = x_{\rm OB}$ from the OB star. This region of thickness d consists of an acceleration zone of size r_0 where suprathermal particles from the stellar wind are accelerated and an adjacent convection zone where particle streaming along the wind contact surface dominates over diffusion. For details see text.

In this case the distance of the shock front from the WR star, $x_{\rm WR}$, and from the OB star, $x_{\rm OB}$, is given by

$$x_{\rm WR} = \frac{1}{1+\sqrt{\eta}} D, \quad x_{\rm OB} = \frac{\sqrt{\eta}}{1+\sqrt{\eta}} D, \tag{2}$$

where

$$\eta = \frac{\dot{M}_{\rm OB} v_{\rm OB}}{\dot{M}_{\rm WR} v_{\rm WR}}, \tag{3}$$

$D = x_{\rm WR} + x_{\rm OB}$ is the separation of the binaries, and $\dot{M}_{\rm OB}$ and $\dot{M}_{\rm WR}$ are the mass-loss rates of the WR and OB star, respectively. Since $\dot{M}_{\rm OB} < \dot{M}_{\rm WR}$ and $v_{\rm OB} \approx v_{\rm WR}$, the shock location is rather close to the OB star, i.e., $D \gg x = x_{\rm OB}$. This appears to be in excellent agreement with the observed locations of the collision region in the radio domain of, e.g., WR 147 (Dougherty et al. 2000), and this also implies that the shocked gas of the winds of both the OB and the WR star have a comparable mass density.

If the wind collision occurs at a distance smaller than the Alfvén radius,

$$r_{\rm A} \approx r_s(1+\xi) \text{ for } \xi \ll 1,$$
$$r_{\rm A} \approx r_s \xi^{1/4} \text{ for } \xi \gg 1,$$

[where $\xi = B_s^2 r_s^2/(2\dot{M} v_\infty)$; B_s is the star's surface magnetic field] from the OB star, significant deceleration of the WR wind in the OB radiation field is expected (Eichler & Usov 1993). In this case, the colliding winds do not reach their terminal velocities. Typically, $\xi \sim 0.01$–0.1, leading to $r_{\rm A} \sim (3r$–$5_s)r_s$ for OB stars (Barlow 1982). For the present work we limit ourselves to situations in which the binary winds reach their terminal velocities at the shock location.

The external magnetic field B of a star changes in an outflow from the classical dipole field,

$$B \approx B_s \left(\frac{r_s}{x}\right)^3,$$

to a radially dominated one at the Alfvén radius,

$$B \approx B_s \left(\frac{r_s^3}{r_{\rm A} x^2}\right),$$

and finally to a toroidally dominated one for $x > r_s v_\infty / v_{\rm rot}$,

$$B \approx B_s \left(\frac{v_{\rm rot} r_s^2}{v_\infty r_{\rm A} x}\right),$$

where $v_{\rm rot}$ is the surface rotation velocity, with typical values of order $\sim 0.1 v_\infty$ for early-type stars (Conti & Ebbets 1977; Penny 1996). We use these equations to determine the magnetic field at the location of the collision front. This value is held constant throughout the emission zone.

The surface magnetic fields of massive stars are not well known. Donati et al. (2002) report the detection of a 1.1 kG bipolar magnetic field of presumably fossil origin at the surface of the young O star θ_1 Ori C. Ignace et al. (1998) argue for surface magnetic field strengths of order 10^4 G in WR stars. On the other hand, from the nondetection of the Zeeman effect for many O and B stars only upper limits of order a few hundred gauss exist (Barker 1986; Mathys 1999). For this work we shall fix the surface magnetic field at a reasonable value of $B_s = 100$ G unless stated otherwise.

The plane of the binary system is inclined by an angle i with respect to the observer ($i = \pi/2$ corresponds to an observer in the plane of the stars), and ϕ_B, the angle between the projected sight line and the line connecting the stars, is a measure of the orbital phase of the system. In the following, periastron passage is defined by the orbital phase $\Phi = 0$, and $\phi_B = 0$ for the WR star being in front of the OB star along the sight line.

In the corotating system centered on the OB star the location of the emission site is defined in polar coordinates by the azimuthal angle ϕ and the polar angle $\theta = \arcsin(r/x) \approx r/x$ for $r \ll x$ (see Fig. 1). In the same star-centered frame the line of sight to the observer is described by the angles ϕ_L, with $\tan\phi_L = \sin\phi_B \cot i$, and θ_L, with $\cos\theta_L = \cos\phi_B \sin i$.

The radiation yield of IC scattering depends on the angle $\theta_{\rm ph} = \theta_{\rm sc}$ between the directions of the incoming (from the OB star) and outgoing photons, which obviously depends on the location of the scattering electron, as well as the orbital phase. We find

$$\mu_{\rm ph} = \cos\theta_{\rm ph} = \cos\theta_L \cos\theta + \sin\theta_L \sin\theta \cos(\phi - \phi_L).$$

The corresponding azimuthal angle $\phi_{\rm ph}$ is irrelevant for the scattering process.

3. PARTICLE SPECTRA

We expect two standing shocks and a discontinuity between them. For typical massive stars the wind velocities are of comparable value, and in addition the ram pressure balance (eq. [1]) ensures a similar upstream gas density for both the OB and the WR wind shocks. It thus appears justified to assume that the two shocks, as well as the corresponding acceleration and escape rates, are identical.

As motivated above, we distinguish two zones of the extended emission region. In the acceleration zone particles of energy E_0 from the stellar winds are energized through diffusive shock acceleration in the test particle approximation at a rate $\dot{E} = aE$, where $a = V_s^2(c_r - 1)/(3c_r\kappa_a)$ (Schlickeiser 2002), where $V_s = v_{\rm OB} = v_{\rm WR}$ is the upstream velocity of the standing shock, c_r is the compression ratio, and κ_a is the (assumed) energy-independent

diffusion coefficient perpendicular to the wind contact surface. For the particle-wave interaction to shape the (power-law) particle distribution from acceleration, E_0 should significantly exceed the thermal particle energy (e.g., Malkov & Völk 1995). In this acceleration region diffusion dominates over the convective flow along the wind contact surface. The acceleration region can, in good approximation, be treated as a leaky box with a free-escape boundary at r_0 (see Fig. 1). Introducing an energy-independent escape time, $T_0 = r_0^2/(4\kappa_d)$, where κ_d is the diffusion coefficient along the wind contact surface, the continuity equation for this zone then reads

$$\frac{\partial}{\partial E}\left[\dot{E}N(E)\right] + \frac{N(E)}{T_0} = Q_0\delta(E - E_0), \tag{4}$$

where $\dot{E} = aE - \dot{E}_{\rm loss}$ includes energy gain through diffusive acceleration as well as continuous energy losses. The detailed energy distribution of the injected particles is of secondary importance for the development of the accelerated particle spectrum but rather depends on the parameters describing the acceleration process. Therefore, we simplify the injection spectrum to a δ-distribution. The solution $N(E)$ consists of a power law that is modified at the high-energy end of the spectrum: $N(E) \propto E^{-s} f_c(E)$, where $f_c(E)$ depends on the radiative energy losses employed and $s = (aT_0)^{-1} + 1$, where energy losses are negligible.

Adjacent to the acceleration zone is the so-called convective zone where convection along the wind contact surface is a faster transport process than is diffusion. For the convective flow we assume for simplicity a constant velocity, $V = pv_{\rm OB}$ with $p = {\rm const} \leq 1$. The continuity equation for this zone also includes adiabatic losses, $\propto E\nabla \boldsymbol{V}$, and is given by

$$\nabla[\boldsymbol{V}N(E,r)] + \frac{\partial}{\partial E}\left[\left(\dot{E} - \frac{E}{3}\nabla\boldsymbol{V}\right)N(E,r)\right] = 0, \tag{5}$$

where $\dot{E} = -\dot{E}_{\rm loss}$ represents the continuous energy losses in this region. The boundary conditions $N(r \rightarrow \infty) = 0$ and $N(r = r_0, E) = N_{\rm acc}(E)$ apply, where $N_{\rm acc}(E)$ is the homogeneous particle density in the acceleration region.

At the location $r = r_0$ the diffusive escape timescale $T_0 = r_0^2/4\kappa_d$ equals the convection timescale $t_{\rm conv} = r_0/V$, and this allows us to determine $r_0 = 4\kappa_d/V$. For the power-law index s, one then finds

$$s = 1 + p^2\frac{3c_r}{4(c_r - 1)}\frac{\kappa_a}{\kappa_d}. \tag{6}$$

It is remarkable that for isotropic diffusion, $\kappa_a = \kappa_d$, s is fully determined by the compression ratio c_r of the shock and the ratio of the convection velocity to the shock velocity. For strong shocks, $c_r = 4$, hard-particle spectra with $s = 1 + p^2$ are then expected in the acceleration zone, while the generic $s = 2$ spectrum requires nonisotropic and/or energy-dependent diffusion, or an extreme value for the convection velocity $V = v_{\rm OB}$. The smallest possible size r_0 of the acceleration region corresponds to the diffusion coefficient κ_d approaching the Bohm limit.

3.1. *Electron Spectra*

The general solution of equation (4) is given by

$$N(E) = \frac{1}{\dot{E}}\int^E dE'\, Q(E') \exp\left[-\frac{1}{T_0}\int_{E'}^E \frac{dE''}{\dot{E}(E'')}\right]. \tag{7}$$

It has been shown that IC scattering, if treated in the Thomson regime, in most cases determines the maximum electron energy and is the most important radiative loss channel for ultrarelativistic electrons in colliding winds of massive stars (Eichler & Usov 1993; Mücke & Pohl 2002), since typically $u_{{\rm ph},T}/u_{\rm B} \geq 1$ ($u_{{\rm ph},T}$ is the energy density of the stellar radiation field, u_B the magnetic field energy density in the emission region). For typical system parameters one finds $u_{{\rm ph},T}/u_B \approx 67 L_{\rm bol,38}/B_{\rm G}^2 x_{\rm OB,13}^2$ where $L_{\rm bol,38}$ is the bolometric luminosity of the OB star in 10^{38} ergs s^{-1}, $B_{\rm G}$ is the magnetic field in the collision region in gauss, and $x_{\rm OB,13} = x_{\rm OB}/(10^{13}$ cm). At lower energies bremsstrahlung and Coulomb scattering determine the shape of the electron spectrum. Radiative losses included in our calculations for the electron spectra are synchrotron losses, IC losses on the stellar radiation field of differential photon density $n_{{\rm ph},T}(\epsilon) = n_0\delta(\epsilon - \epsilon_T)$ (monochromatic approximation), electron-ion bremsstrahlung, and Coulomb losses. We do not separately consider ionization losses on cold matter or heavy atoms, as those scale very similar to the Coulomb losses, if the impacting particle is much faster than the orbital electron.

The total radiative energy loss rate is then given by

$$\dot{E} = -(b_{\rm syn} + b_{\rm IC,TL})E^2 + (a - b_{\rm br})E - b_{\rm coul}, \tag{8}$$

with

$$b_{\rm IC,TL} = \frac{4}{3m_e^2c^3}\sigma_{\rm T}u_{\rm ph}$$

for the Thomson regime, where c is the velocity of light, $\sigma_{\rm T} = 6.65 \times 10^{-25}$ cm^2 is the Thomson cross section,

$$b_{\rm syn} = \frac{4}{3m_e^2c^3}\sigma_{\rm T}u_B,$$

$$b_{\rm br} = \frac{2}{\pi}\alpha\sigma_{\rm T}cN_{\rm H}$$

in the weak-shielding limit where we have neglected the logarithmic term, α is the fine-structure constant, m_e is the electron mass, $N_{\rm H}$ is the thermal ion density (in particles per cubic centimeter), and (Schlickeiser 2002)

$$b_{\rm coul} = 55.725c\sigma_{\rm T}N_{\rm H}m_ec^2.$$

Figure 2 shows the energy loss rates in comparison to the acceleration rate for a set of parameters typically found for colliding wind binaries. Obviously, Coulomb losses dominate the low-energy end of the electron spectrum and simultaneously provide a lower limit to the acceleration rate a. At energies $E \gtrsim m_e^2c^4/\epsilon_T$ Klein-Nishina effects significantly modify the energy loss rate due to IC scattering. Figure 2 demonstrates that, first, Klein-Nishina effects can, in general, not be neglected in the environment of colliding massive star winds. Second, the curvature of the loss rate due to the Klein-Nishina decline of the IC cross section actually starts already at much lower electron energies. Consequently, in some cases the electron spectrum might be rather limited by synchrotron losses if the wind parameters are favorable. In the following, we take into account Klein-Nishina effects already above $E > E_{\rm TL}$, where $E_{\rm TL}$ is considered the energy below which the Klein-Nishina energy loss deviates no more than 20%–25% from the Thomson limit approximation. Typically, for the systems considered in this work $E_{\rm TL} \approx 10^{-2}$ MeV/$\epsilon_{T,{\rm MeV}}$ with $\epsilon_{T,{\rm MeV}}$ the target photon energy in MeV.

In the extreme Klein-Nishina regime the total electron energy losses in the acceleration zone at high energies are effectively

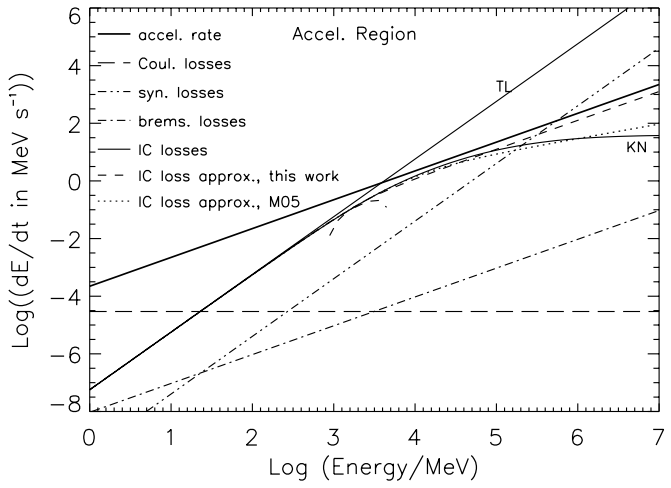

FIG. 2.—Energy loss rates due to IC scattering (*thin solid lines*) in the Thomson regime (TL) and Klein-Nishina regime (KN), synchrotron radiation (*double-dot–dashed line*), relativistic electron-ion bremsstrahlung (*dash-dotted line*), and Coulomb interactions (*dashed line*) in comparison to the acceleration rate (*thick solid line*) in the acceleration zone. The dashed line represents the IC loss approximation used in this work; the corresponding approximation from Moderski et al. 2005 (M05) is shown as a dotted line. Parameters are $L_{\rm bol,OB} = 10^5\,L_\odot$, $\epsilon_T = 10$ eV, $\dot{M}_{\rm OB} = 10^{-6}\,M_\odot\,{\rm yr}^{-1}$, $\dot{M}_{\rm WR} = 10\dot{M}_{\rm OB}$, $v_{\rm OB} = 3768\,{\rm km\,s^{-1}}$, $D = 10^{14}$ cm, $B_s = 100$ G, $x_{\rm OB} \approx 0.24D$, $B \approx 0.5$ G, $n_{{\rm ph},T} \approx 10^{11}$ cm^{-3}, $N_{\rm H} \approx 5\times10^7$ cm^{-3}, $\kappa_a = 1.6\times10^{20}$ cm^2 s^{-1}, $V \approx 1884$ km s^{-1}, $T_0 \approx 1127$ s, and $r_0 \approx 8.5\times10^{11}$ cm.

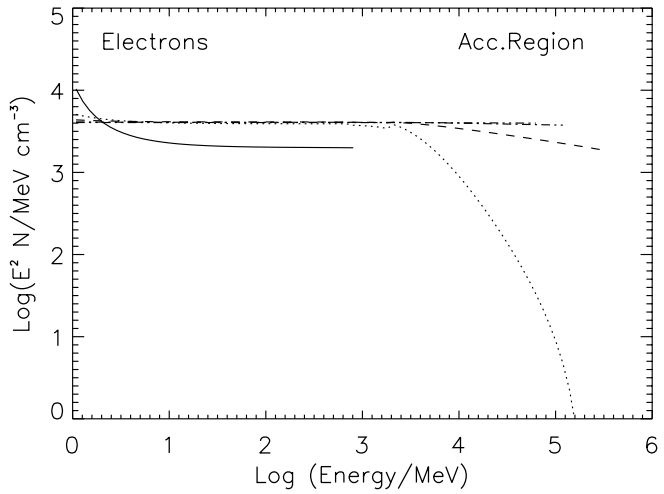

FIG. 3.—Steady state electron spectrum in the acceleration region for $D = 5\times10^{13}$ cm (*solid line*), 10^{14} cm (*dotted line*), 2×10^{14} cm (*dashed line*), 5×10^{14} cm (*dash-dotted line*), and 10^{15} cm (*double-dot–dashed line*). Parameters are $Q_0 = 1$ cm^{-3} s^{-1}, $E_0 = 1$ MeV, $B \approx 1.3$, 0.5, 0.30. 1, and 0.05 G, $n_{{\rm ph},T} \approx (44, 11, 2.8, 0.4, 0.1)\times10^{10}$ cm^{-3}, $N_{\rm H} \approx (21, 5.2, 1.3, 0.2, 0.05)\times10^7$ cm^{-3}, $v_{\rm OB} = 3537$, 3768, 3884, 3954, and 3977 km s^{-1}, $V \approx 1768$, 1884, 1942, 1977, and 1988 km s^{-1}, and $r_0 \approx (9, 8.5, 8.2, 8.1, 8)\times10^{11}$ cm. All other parameters are the same as in Fig. 2.

only provided by synchrotron radiation. In the transition range between the Thomson and Klein-Nishina limit, however, IC scattering may still dominate over synchrotron emission, thus mandating a proper treatment of the former. To allow for analytical solutions of equation (4), we approximate the Klein-Nishina decline of the loss rate in the transition range by

$$\dot{E}_{\rm IC,KN} = -b_{\rm IC,TL}E^2\left(1 - \frac{E\epsilon_{T,\rm MeV}}{5\times10^{-2}\ \rm MeV}\right) \qquad (9)$$

for all energies $E < E_s = (10^{-1.7}$ to $10^{-1.6})$ MeV$/\epsilon_{T,\rm MeV}$, and

$$\begin{aligned}\dot{E}_{\rm IC,KN} &\simeq -\,(0.27\sigma_{\rm T}cn_{{\rm ph},T}\epsilon_{T,\rm MeV}^{1/8}E + 7\epsilon_{T,\rm eV}^{-1.846}D_{14}^{-2} \\ &\quad + 2.1\times10^{-4})\ {\rm MeV\ s^{-1}} \\ &= -\,(q_aE + q_b) \end{aligned} \qquad (10)$$

for $E \geq E_s$, with $n_{{\rm ph},T}$ as the integrated target photon density and D_{14} the binary separation in 10^{14} cm. These approximations are tested for $\epsilon_T = 1$–100 eV and are suitable for $0.01u_{{\rm ph},T} \leq u_B \leq u_{{\rm ph},T}$ (while they deviate by more than an order of magnitude at energy $q_a/(2b_{\rm syn})\{1 + \left[(1 - 4b_{\rm syn}q_b/q_a^2)\right]^{1/2}\}$ if u_B decreases to $\leq 0.003u_{{\rm ph},T}$).

This approximation is indicated in Figure 2 by the long-dashed line and is suitable when relativistic bremsstrahlung losses are much smaller than synchrotron or IC losses. While this approach takes reasonably into account the early deviation of the Klein-Nishina cross section from the Thomson cross section, it overestimates the energy loss rate in the extreme Klein-Nishina regime, which is mainly responsible for the steepness of the declining electron spectrum. Consequently, our derived electron and photon spectra shall be used with caution in their declining part. In Figure 2 we compare our approximation with the one recently derived by Moderski et al. (2005). While both approximations are in very good agreement in the Klein-Nishina transition region, the approach of Moderski et al. (2005) resembles more closely the exact formula at higher energies. Considering the limitations in electron energy discussed below and to keep the electron continuity equations analytically solvable, we use equations (9) and (10) for the present work.

The quantity E_0 represents the lower limit for the resulting particle distribution in the acceleration zone. In order to allow the representation of elastic Coulomb scattering as a continuous loss term and relativistic approximations for loss rates to be applicable, we use $E_0 = 1$ MeV in the following, if not noted otherwise.

The analytical solutions of equation (4) for electrons in the acceleration region are detailed in Appendix A. Figure 3 shows examples of the resulting electron spectra for various values of the binary separation, while all other parameters are the same as used in Figure 2. The general shape is determined by the interplay between acceleration gains and losses. At low energies Coulomb losses dominate and lead to the well-known upturn toward low energies due to the stronger increase of the acceleration rate with energy $\dot{E}_{\rm acc} \propto E$ when comparing to the competing radiative losses $\dot{E}_{\rm loss} \propto$ const. For a reasonable convection velocity $V = 1/2v_{\rm OB}$ (e.g., Luo et al. 1990) and assuming strong shocks $c_r = 4$, an $\propto E^{-2}$ particle spectrum develops in the acceleration region if $\kappa_a/\kappa_d = 4$, which we shall use in the following for demonstrative purposes if not noted otherwise. Thus, in Figure 3 an E^{-2} spectrum develops until IC losses cause a steepening. The shape of this decline reflects the approximation employed to simulate the losses in the Klein-Nishina regime. The kink at $\sim10^{3.5}$ MeV corresponds to the transition from the Thomson regime to the Klein-Nishina loss rate approximation. Finally, the cutoff at energy E_c can be either due to radiative losses dominating over the acceleration rate, or the diffusion coefficient κ_d approaching the Bohm limit $\kappa_{\rm Bohm} \approx 1/3r_{\rm L}c$, where $r_{\rm L}$ is the Larmor radius. In the latter case the escape timescale T_0 decreases with energy. For simplicity (and in order to keep the solutions analytical) we set $T_0 = 0$ at $\kappa_d \leq \kappa_{\rm Bohm}$, which then causes a sharp cutoff. More sophisticated calculations may smooth this decline toward an approximately exponential shape (Protheroe & Stanev 1999). In the former case the cutoff is determined by

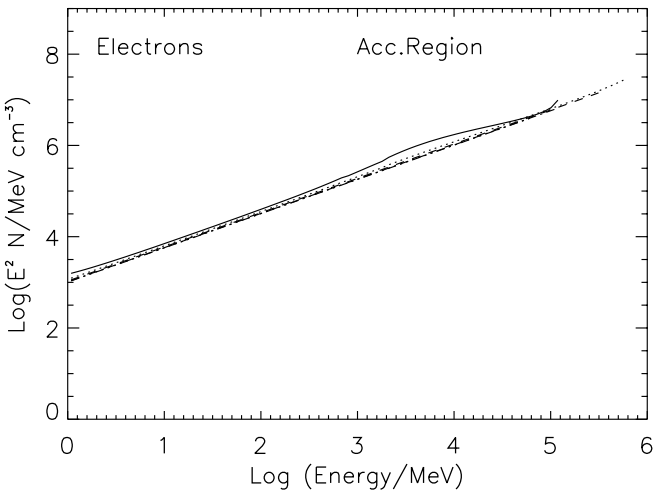

FIG. 4.—Steady state electron spectrum in the acceleration region assuming $\kappa_a = \kappa_d = 4 \times 10^{19}$ cm^2 s^{-1} and for $D = 5 \times 10^{13}$ cm (*solid line*), 10^{14} cm (*dotted line*), 2×10^{14} cm (*dashed line*), 5×10^{14} cm (*dash-dotted line*), and 10^{15} cm (*double-dot–dashed line*). All other parameters are the same as in Fig. 3.

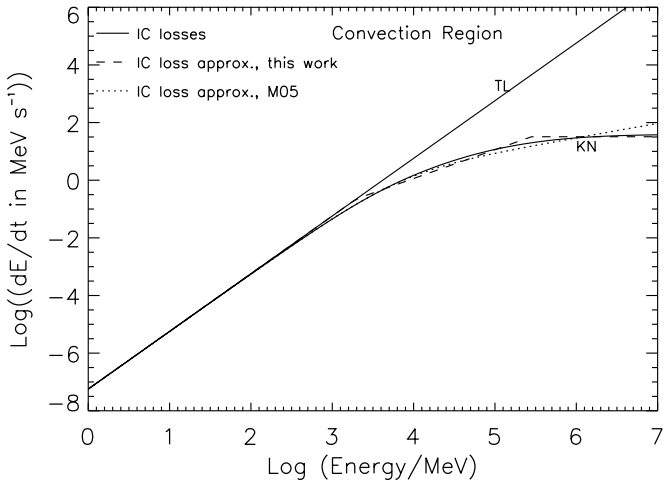

FIG. 5.—Energy-loss rates in the convection zone due to IC scattering in the Thomson regime (TL, *thin solid lines*) and the Klein-Nishina regime (KN). The dashed line represents the IC loss approximation employed in this work, which is compared to the approximation used in Moderski et al. 2005 (M05; *dotted line*). The parameters are the same as in Fig. 2.

the synchrotron loss rate that dominates when regarding the flattening loss curve at high energies. In Figure 3 the particle spectra cutoff is due to radiative losses for $D \leq 10^{14}$ cm, while at larger binary separations the Bohm limit causes the cutoff. Here both synchrotron and IC losses cease to be able to significantly affect the acceleration spectrum. For comparison we have also calculated electron spectra assuming isotropic diffusion. Figure 4 shows the resulting spectra in which all parameters are unchanged with respect to Figure 3 except for the ratio of the diffusion coefficients κ_a/κ_d. As expected, hard-particle spectra with spectral index $s = 1 + p^2 = 1.25$ develop, and radiative losses alter the spectral shape depending on the binary separation. For $E \rightarrow E_c$ the spectra diverge for $[(a - b_{\rm br})T_0]^{-1} < 1$ (see eqs. [A1] and [A2]), which is fulfilled here.

Generally, we find that the electron spectrum cuts off at energies that do not permit significant TeV-band γ-ray emission. At first glance this may appear at odds with the recent detection of TeV-scale emission from the X-ray binary LS 5039 (Aharonian et al. 2005b) and the binary system PSR 1259−63/SS 2883 (Aharonian et al. 2005a). One should note, however, that the cutoff energy strongly depends on the magnetic field strength and on the geometry of the wind collision zone, both of which are expected to be different for microquasars and pulsar binaries.

The cutoff energy may also be enhanced by a runaway streaming instability in the acceleration region, which would amplify the magnetic field, and hence reduce the Bohm diffusion coefficient (Lucek & Bell 2000; Bell & Lucek 2001). The process has been proposed to operate near the forward shocks of supernova remnants, but the observational evidence is controversial. Conservatively, we do not consider magnetic field amplification here.

Figure 5 shows the energy loss rates in the convection zone for the same parameters as used for Figure 2. On account of expansion in the cylindrical convection flow the magnetic field strength and the gas density fall off quickly with distance from the acceleration region. Coulomb interactions, bremsstrahlung, and synchrotron radiation will therefore lose importance as energy loss mechanisms, and the IC scattering effectively provides the bulk of the electron energy losses.

Using a constant convection velocity, the steady state particle spectrum in the convection region can be found by solving equation (5). With the boundary conditions $N(E, r) \rightarrow 0$ for $r \rightarrow \infty$ and $N(E, r) \rightarrow N_{\rm acc}(E)$ for $r \rightarrow r_0$, where $N_{\rm acc}(E)$ is the steady state particle spectrum in the acceleration region, we derive the following analytical solutions using the standard method of characteristics: For $E < E_{\rm TL}$ the radiative losses are $\dot{E} = -b_{\rm syn\&IC}E^2$ and

$$N(E) = \left(\frac{r_0}{r}\right)^{2/3} \left\{1 + \frac{3b_{\rm syn\&IC}}{2V} Er\left[\left(\frac{r_0}{r}\right)^{2/3} - 1\right]\right\}^{-2} N_{\rm acc}(\tilde{E}), \tag{11}$$

with

$$\tilde{E} = E\left(\frac{r}{r_0}\right)^{1/3} \left\{1 + \frac{3b_{\rm syn\&IC}}{2V} Er\left[\left(\frac{r_0}{r}\right)^{2/3} - 1\right]\right\}^{-1}. \tag{12}$$

For $E \geq E_{\rm TL}$ an analytical solution cannot be found using equation (9). In the convection region the approximation for the IC energy losses in the Klein-Nishina regime, $E > E_{TL}$,

$$\dot{E}_{\rm IC,KN} = -q_c E, \tag{13}$$

for $E_{\rm TL} < E < E_{\rm extr}$, with $q_c \approx b_{\rm IC}E_{\rm TL}$, and

$$\dot{E}_{\rm IC,KN} = -q_d, \tag{14}$$

for $E \geq E_{\rm extr} = q_d/q_c$, with $q_d \approx 9/16 c\sigma_{\rm T} m_e^2 c^4 n_{{\rm ph},T}\epsilon_T^{-1}$, turns out to be reasonable if $E_{\rm TL}$ is increased to $E_{\rm TL} \approx 10^{-1.7}{\rm MeV}/\epsilon_{T,{\rm MeV}}$ (see Fig. 5). As shown in Figure 5, a comparison of this approximation with that given in Moderski et al. (2005) reveals good agreement, with the approach taken in this work being more realistic in the extreme Klein-Nishina regime. Again, the cited approximation leads to an analytically unsolvable continuity equation. Using equations (13) and (14), the solution of equation (5) is

$$N(E) = \exp\left[\frac{q_c}{V}(r - r_0)\right]\left(\frac{r_0}{r}\right)^{2/3} N_{\rm acc}(\tilde{E}), \tag{15}$$

with

$$\tilde{E} = E\exp\left[\frac{q_c}{V}(r - r_0)\right]\left(\frac{r}{r_0}\right)^{1/3}, \tag{16}$$

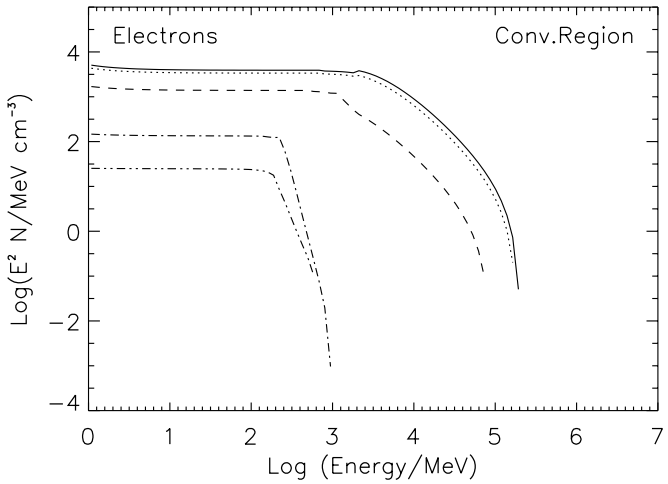

FIG. 6.—Steady state electron spectra in the convection region at distance $\Delta r = 10^{11}$ cm (*dotted line*), 10^{12} cm (*dashed line*), 10^{13} cm (*dash-dotted line*), and 5×10^{13} cm (*double-dot–dashed line*) from the transition point r_0, as compared to the electron spectrum in the acceleration region (*solid line*) and for a binary separation of $D = 10^{14}$ cm. All other parameters are the same as in Fig. 2.

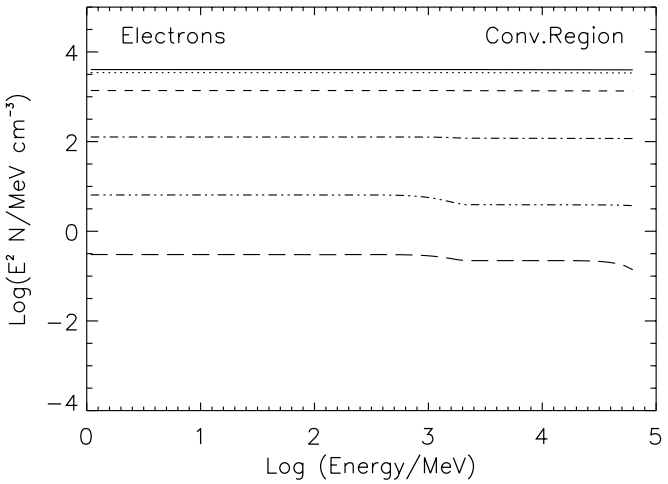

FIG. 7.—Same as in Fig. 6, but for a binary separation of $D = 10^{15}$ cm and $\Delta r = 10^{11}$ cm (*dotted line*), 10^{12} cm (*short-dashed line*), 10^{13} cm (*dash-dotted line*), 10^{14} cm (*double-dot–dashed line*), and 10^{15} cm (*long-dashed line*).

for $E_{\rm TL} < E < E_{\rm ext}$, and

$$N(E) = \left(\frac{r_0}{r}\right)^{2/3} N_{\rm acc}(\tilde{E}), \tag{17}$$

with

$$\tilde{E} = E\left(\frac{r}{r_0}\right)^{1/3} + \frac{3q_d}{4V}\left[\left(\frac{r}{r_0}\right)^{1/3} r - r_0\right], \tag{18}$$

for $E \geq E_{\rm ext}$. The total solution is then combined such to assure continuity for all functions $E(r)$, $N(E, r, r_0, N_{\rm acc}(\tilde{E}))$.

Figure 6 shows the resulting electron spectrum in the convection region at $r = r_0$ to 10^{14} cm with a binary separation of $D = 10^{14}$ cm and using the parameters as described in Figure 2 for the acceleration region. As the particles convect along r, radiative losses alter the high-energy end of the particle spectrum, leading to a decreasing cutoff energy with increasing r, while adiabatic losses lower the overall particle density. In Figure 7 the binary separation has been enlarged to $D = 10^{15}$ cm. As a result, radiative losses show a significant impact on the spectral shape only at large r.

In summary, taking into account convection in the extended emission region alters the energy cutoff in the integrated particle spectrum if radiative losses prove to be important and simultaneously lowers the total nonthermal particle density. This behavior is reflected in the corresponding photon spectra (see § 4).

3.2. *Proton Spectra*

If protons are accelerated together with the electrons, hadronic nucleon-nucleon interaction takes place with an approximated energy loss rate of

$$\dot{E} = -b_{\rm pp} E \tag{19}$$

above the kinematic threshold for pion production $E > E_{\rm thr} \simeq 0.28$ GeV,

$$b_{\rm pp} = 1.3 \times 3 c N_{\rm H} \sigma_{\rm pp} \frac{m_\pi}{m_p}, \tag{20}$$

where $\sigma_{\rm pp} = 3 \times 10^{-26}$ cm^2 is the corresponding hadronic cross section, and the factor 1.3 takes into account the assumed abundance (90% H, 10% He). Note that this linear relation for the energy loss rate is exact only above a nucleon kinetic energy of a few GeV, whereas at lower energies it is considered as an approximation. The corresponding error drops below ~30% above ~10 GeV. In addition, Coulomb losses in the dense wind of the massive companion star of the WR star will alter the injection spectrum. The Coulomb losses are

$$\dot{E} = -\frac{3 c \sigma_{\rm T} m_e c^2 Z^2 \ln\lambda}{2} N_{\rm H} \frac{\beta^2}{x_m^3 + \beta^3}, \tag{21}$$

with

$$\beta = \frac{\sqrt{E(E + 2 m_p c^2)}}{E + m_p c^2}$$

and

$$x_m = 0.2 \sqrt{\frac{T_e}{10^8 \text{ K}}}.$$

The Coulomb barrier occurs at $E_m \simeq 20$ MeV$(T_e/10^8$ K), where $T_e \approx 10^8$ K is the electron temperature. We approximate the Coulomb losses by

$$\dot{E} = -b_{\rm bel} E_{\rm MeV} \tag{22}$$

below the Coulomb barrier, with $b_{\rm bel} = 6.6 \times 10^{-16} Z^2 N_{\rm H} / x_m^3$ MeV s^{-1}, $E_{\rm MeV}$ is the particle kinetic energy in MeV, and

$$\dot{E} = \frac{-b_{\rm ab}}{\sqrt{E_{\rm MeV}}} \tag{23}$$

above the Coulomb barrier, with $b_{\rm ab} = 6.7 \times 10^{-12} Z^2 N_{\rm H}$ MeV s^{-1}. This approximation deviates at most by a factor of ~2 (by approaching the Coulomb barrier) from the exact loss formula. In the relativistic regime, $\beta \geq 0.5$, we use

$$\dot{E} = -b_{\rm rel}, \tag{24}$$

with $b_{\rm rel} = 3.1 \times 10^{-13} Z^2 N_{\rm H}$ MeV s^{-1}.

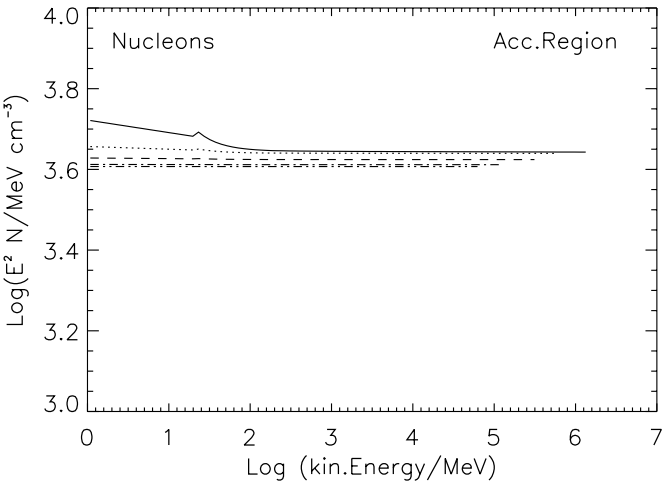

FIG. 8.—Steady state proton spectra in the acceleration region for binary separations $D = 5 \times 10^{13}$ cm (*solid line*), 10^{14} cm (*dotted line*), 2×10^{14} cm (*dashed line*), 5×10^{14} cm (*dash-dotted line*), and 10^{15} cm (*double-dot–dashed line*). The quantity Q_0 is set to unity, $E_{0,\mathrm{kin}} = 1$ MeV, and $T_e = 10^8$ K. All other parameters are the same as in Fig. 3.

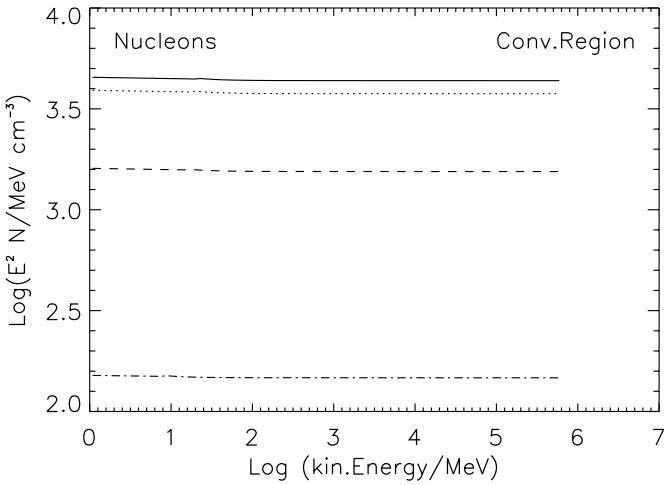

FIG. 9.—Steady state proton spectra in the convection region at distance $\Delta r = 10^{11}$ cm (*dotted line*), 10^{12} cm (*dashed line*), and 10^{13} cm (*dash-dotted line*) from the transition point r_0, as compared to the proton spectrum in the acceleration region (*solid line*) and for a binary separation of $D = 10^{14}$ cm. All other parameters are the same as in Fig. 8.

Equation (4) describes the behavior of the steady state spectrum in the acceleration region. The solution, equation (7), can again be derived analytically (see Appendix B).

Figure 8 shows examples of steady state nucleon spectra with varying distance of the binary stars to each other. Close binaries show an upturn at low energies due to a high rate of Coulomb losses, and a spectral shape at larger energies that repeats the acceleration spectrum due to the same energy dependence of losses from hadronic *pp*-interactions and energy gain. For large binary separations Coulomb losses are unimportant, and the loss-corrected particle spectrum has the same spectral shape as the steady state acceleration spectrum. Due to the low hadronic cross section, radiative losses hardly cause any cutoff in the particle spectrum. Instead, faster particle escape when approaching the Bohm diffusion limit leads to a steepening of the emitting particle distribution. For simplicity, we chose to treat this effect analogously to the electron acceleration in § 3.1, i.e., we set $T_0 = 0$ for $\kappa_d \leq \kappa_{\mathrm{Bohm}}$.

Applying mass conservation, the continuity equation implies $N_{\mathrm{H}} \propto r^{-1}$ for the target ion density N_{H}. With $r > r_0$, where r_0 indicates the transition from the acceleration to convection region with typically $r_0 \sim 10^{12}$ cm in the star systems considered here, hadronic *pp*-interactions and Coulomb losses can readily be neglected. Equation (5) can be solved to give the analytical solution for a constant convection velocity V:

$$N(E) = \left(\frac{r_0}{r}\right)^{2/3} N_{\mathrm{acc}}(\tilde{E}), \tag{25}$$

with

$$\tilde{E} = E\left(\frac{r}{r_0}\right)^{1/3}. \tag{26}$$

Figure 9 shows the resulting nucleon spectrum for the same parameter set as used in Figure 6. Obviously the losses due to *pp*-interactions are of minor importance compared to the adiabatic losses the nucleons suffer in the convection region.

3.3. *Particle Spectra Normalization*

For applications to massive stars in binary systems the normalization of the relativistic particle component is limited by several constraints: First, the IC, bremsstrahlung, and π^0-decay γ-rays must not exceed any limits imposed by γ-ray observations. Second, since the particles are accelerated out of the pool of thermal particles; particle number conservation dictates that the relativistic particle flux injected into the system must be smaller than the wind particle flux entering the acceleration zone, i.e., $Q_0 \leq \dot{M}/(m_p x^2 4\pi d)$, with d the thickness of the acceleration site. Furthermore, due to energy conservation, the total injected particle energy cannot be larger than the total kinetic wind energy of the binary system, which rarely exceeds 1% of the total radiative energy output of the stars (typically $L_w \leq 10^{37}$ ergs s^{-1}). The energy density of accelerated particles is given by $U_{\mathrm{acc}} \approx Q_0 E_0/a$, assuming an E^{-2} spectrum ($aT_0 = 1$). In equilibrium the total acceleration power equals the loss power due to escape, leading to $L_{\mathrm{acc}} = U_{\mathrm{acc}} V_{\mathrm{acc}}/T_0$, where $V_{\mathrm{acc}} = r_0^2 \pi d$ is the acceleration volume. By noting that $(r_0^2/4x^2)L_w$ is the kinetic power available to the acceleration region, Q_0 cannot exceed $Q_0 \sim (r_0^2/4x^2)L_w/(V_{\mathrm{acc}}E_0) = L_w/(4x^2\pi d E_0)$. These latter two arguments pose to date a more severe constraint on the normalization than the γ-ray observations from EGRET. In the following we use this maximum possible injection power unless stated otherwise.

4. PHOTON SPECTRA

This work is devoted to photon emission at high energies with emphasis on the $\geq$1 MeV regime. Important nonthermal continuum emission processes considered here are IC scattering of the dense stellar radiation field to high energies, relativistic bremsstrahlung of the electrons in the field of the ions in the wind, and the decay of $\pi^0 \longrightarrow \gamma + \gamma$ that are produced in hadronic nucleon-nucleon collisions. For the calculations of the photon spectra we assume the particle distributions to be isotropic in the wind-wind collision zone.

4.1. *Inverse Compton Scattering*

IC scattering in the dense UV stellar radiation field of the massive main-sequence star often dominates photon production rate at high energies. The computation of the photon emission is based on the full Klein-Nishina cross section, while for the IC losses of the electrons either the cross section in the Thomson

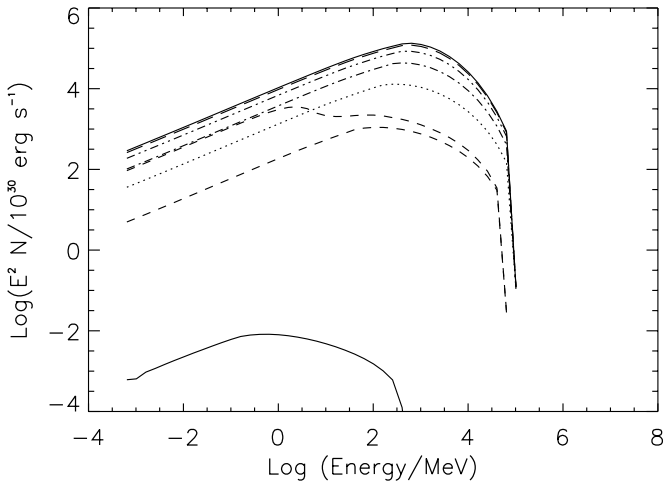

FIG. 10.—IC spectra from the acceleration region for $D = 10^{14}$ cm and $\theta_L = 0^\circ$ (*lower solid line*), 30° (*lower dashed line*), 60° (*dotted line*), 90° (*dash-dotted line*), 120° (*double-dot–dashed line*), 150° (*long-dashed line*), and 180° (*upper solid line*). The normalization corresponds to a injected power of particles with energy $E_0 = 1$ MeV prior to acceleration of $\sim$0.031% of the total OB wind luminosity; the emitting volume is $\sim 5 \times 10^{37}$ cm^3. For $\theta_L = 30^\circ$ the total volume-integrated (i.e., acceleration plus convection zone) IC spectrum is also shown (*upper dashed line*). All parameters except for D are the same as used in Fig. 3. The thickness d of the emission region is estimated by $d \approx x = x_{\rm OB}$ (Eichler & Usov 1993).

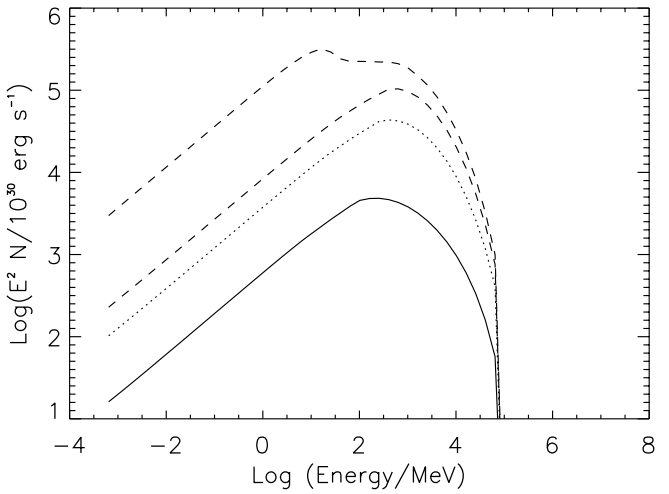

FIG. 11.—IC spectra from the acceleration region for $D = 10^{14}$ cm, inclination angle $i = 45^\circ$ and $\Phi_B = 0^\circ$ (*solid line*), 90° (*dotted line*), and 180° (*lower dashed line*). For $\Phi_B = 180^\circ$ the total volume-integrated (i.e., acceleration plus convection zone) IC spectrum is also shown (*upper dashed line*). We define $\Phi_B = 0$ for the WR star being in front of the OB star. All other parameters are the same as used in Fig. 10.

limit or the Klein-Nishina approximation equations (9), (10), and (13) are applied assuming the losses to be continuous. We have further neglected triplet pair production (TPP). The value of $\epsilon_T E/(m_e c^2)^2$ that we consider hardly reaches 10–100, well below the critical value of $\sim 10^5$–10^6 (Mastichiadis 1991; Dermer & Schlickeiser 1991) for which TPP dominates over IC scattering. In some cases its energy threshold is not even reached. We restrict this work to long-period binary systems, for which the wind momentum from the WR star clearly dominates, thus placing the WR star at a large distance from the collision region. This allows us to neglect the stellar radiation field of the WR star as a target photon field for IC scattering. For the stellar radiation field of the OB star the monochromatic approximation,

$$n(\epsilon, \mu_{\rm ph}) = n_0 \delta(\epsilon - \epsilon_T)\delta(\mu - \mu_{\rm ph}), \tag{27}$$

with $\epsilon_T = 2.7 k_{\rm B} T_{\rm eff}$ is employed. All seed photons are approaching the emission region from the same direction. In this case the full angular dependence of the IC scattering rate has to be taken into account, since the scattered power per volume element depends on the scattering angle $\theta_{\rm ph}$. In Appendix C we calculate the IC photon production rate, $\dot{n}(\epsilon_s, \Omega_s)$, for an arbitrary target photon field $n(\epsilon, \mu_{\rm ph})$ that scatters off an isotropic electron distribution. We find a declining scattering rate with decreasing scattering angle $\theta_{\rm ph}$, in agreement with earlier works (Reynolds 1982; see Fig. C.1 of Brunetti 2000). The volume-integrated emitted photon power is calculated by

$$\dot{N}_{\rm IC}(\epsilon_s) = \int dV\, \dot{n}(\epsilon_s, \Omega_s) = d \int dr\, r \int d\phi\, \dot{n}(\epsilon_s, \Omega_s), \tag{28}$$

where the integrals have been solved numerically. The IC flux variations directly translate into a change of IC power and maximum energy with viewing angle $\theta_{\rm ph}$ (see Fig. 10). For a given system inclination the total emitted power and maximal scattered energy therefore varies with orbital phase (Fig. 11). These anisotropy effects may exhibit detectable patterns in observations with γ-ray instruments like *GLAST* (see § 6). For a non-negligible size of the convection zone, the volume integration may lead to photon spectra that show a kink. This feature occurs at energies above which the convection zone is lacking high-energy particles. The combined effect of both a deficit of high-energy particles in the convection zone and a visible increase of the total flux from the convection zone results in the kink at 1–10 MeV in Figures 10 and 11.

4.2. *Relativistic Bremsstrahlung*

Nonthermal relativistic bremsstrahlung losses are non-negligible in the stagnation point of the colliding winds where the (compressed) gas density may reach values of 10^5–10^9 cm^{-3}, whereas in the convection region the decreasing gas density makes its contribution minor. The nonthermal bremsstrahlung photon flux using a typical interstellar medium metallicity (90% H, 10% He, neglecting contributions from higher atomic number particles),

$$\dot{N}_{\rm ph,br}(E_\gamma) = \frac{1.3 N_{\rm H} c}{4\pi d_L^2} \int dV \int_{\max(E_\gamma m_e c, E_{\rm min})}^{E_{\rm max}} dE\, N(E) \frac{d\sigma}{dE_\gamma}, \tag{29}$$

is calculated numerically in the relativistic limit (valid for $E/m_e c^2 \geq 15/Z$, Z is the atomic number) using the differential cross section from Blumenthal & Gould (1970). Examples of bremsstrahlung spectra are shown in Figure 12 for the electron spectra in Figure 3. The shape of the bremsstrahlung photon spectrum in the relativistic regime reflects the shape of the electron spectrum. The larger the binary separation is, the larger is the difference between the turnover energy from the Thomson to Klein-Nishina loss regime and the cutoff energy (see Fig. 3). This leads to a decline of the bremsstrahlung spectrum at an energy that increases with the binary separation. An estimate of the thickness d of the emission region was provided by Eichler & Usov (1993), who showed that $d \approx x = x_{\rm OB}$. With $r_0 \approx 10^{12}$ cm, the total emitting volume in the acceleration region is

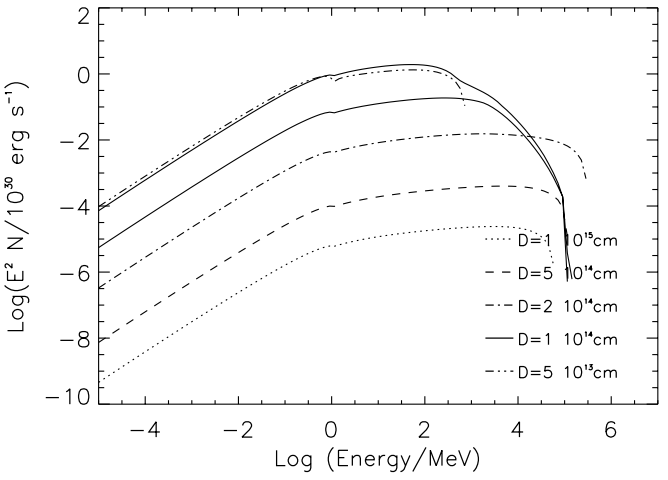

FIG. 12.—Relativistic bremsstrahlung spectra from underlying electron distributions, as presented in Fig. 3 for various binary separations $D = 5 \times 10^{13}$ cm (*double-dot–dashed line*), 10^{14} cm (*lower solid line*), 2×10^{14} cm (*dash-dotted line*), 5×10^{14} cm (*dashed line*), and 10^{15} cm (*dotted line*), emitted from the acceleration region. The normalization corresponds to a injected power of particles with energy $E_0 = 1$ MeV of ~0.14%, 0.031%, 0.007%, 0.001%, and 0.0003%, respectively, of the total OB wind luminosity. The emitting volume varies between 3×10^{37}–5×10^{38} cm^3. The upper solid line corresponds to the sum of bremsstrahlung emission from acceleration and convection region (up to $\Delta r = 10^{13}$ cm) for a binary separation of $D = 10^{14}$ cm, while the lower one corresponds to the acceleration region only.

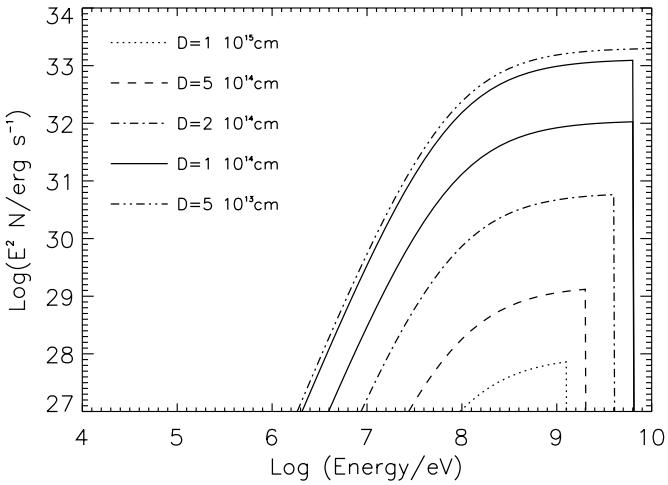

FIG. 13.—The π^0-decay γ-ray spectra from underlying proton distributions as presented in Fig. 8 for various binary separations $D = 5 \times 10^{13}$ cm (*double-dot–dashed line*), 10^{14} cm (*lower solid line*), 2×10^{14} cm (*dash-dotted line*), 5×10^{14} cm (*dashed line*), and 10^{15} cm (*dotted line*), emitted from the acceleration region. The normalization corresponds to a injection power of ~0.14%, 0.031%, 0.007%, 0.001%, and 0.0003%, respectively, of the total OB wind luminosity in form of thermal particles of energy $E_{0,\mathrm{kin}} = 1$ MeV. The emitting volume varies between 3×10^{37} and 5×10^{38} cm^3. The upper solid line corresponds to the sum of π^0-decay photon emission from acceleration and convection region (up to $\Delta r = 10^{13}$ cm) for a binary separation of $D = 10^{14}$ cm.

$\pi r_0^2 d \approx 10^{38}$–$10^{39}$ cm^3. Figure 12 shows the resulting relativistic bremsstrahlung power spectra for various binary separations. Despite a somewhat larger emitting volume for colliding wind systems with a large binary separation, the total bremsstrahlung emission declines with binary separation due to a rapidly decreasing target gas density in the collision region. For $D = 10^{14}$ cm, the compound acceleration and convection region spectrum is also presented in Figure 12. Due to the volume effect, the dominant contribution to the total emission spectrum comes from the convection region at large r, thus increasing the overall bremsstrahlung intensity. At the same time the deficit of high-energy particles in the convection region at large distances from the acceleration region (see Fig. 6) leads to a deficit of high-energy photons. This causes the feature at ~100 MeV in the total bremsstrahlung spectrum shown in Figure 12 (plotted for a $D = 10^{14}$ cm binary separation).

4.3. π^0-Decay γ-Ray Emission

Collisions between cosmic-ray protons and nucleons in massive star winds are rather rare and occur on average a few times per year for gas densities in the wind collision region typical for long-period binaries like WR 140. The stationary proton spectra, as shown in Figures 8 and 9, are used to calculate the π^0-decay photon spectrum. The differential photon flux is given by

$$N_{\mathrm{ph},\pi}(E_\gamma) = 2 \int_{E_\gamma + m_\pi^2 c^4 / 4E_\gamma}^{\infty} dE_\pi \, \frac{N_\pi(E_\pi)}{\sqrt{E_\pi^2 - m_\pi^2 c^4}},$$

with

$$N_\pi(E_\pi) = c N_{\mathrm{H}} \int_{\max\left(E_{\mathrm{thr}}, E_{p,\min}\right)}^{E_{p,\max}} dE_p \, \beta N_p(E_p) \frac{d\sigma_\pi(E_\pi, E_p)}{dE_\pi},$$

where $N_p(E_p)$ denotes the proton spectrum at energy E_p, which is valid in a range $E_{p,\min} \le E_p \le E_{p,\max}$, and σ_π is the production cross section for π^0. Since the proton spectra above the threshold for pp-interactions in general reflects the shape of the acceleration spectrum, one expects pure power-law particle spectra in this energy range. The formalism developed by Pfrommer & Ensslin (2004) for the π^0-decay γ-ray production of pure power-law particle spectra seems therefore appropriate to use. The resulting π^0-decay γ-ray spectra (calculated for a ^{4}He mass fraction of 0.3 for the wind metallicity; see § 4.2) from the acceleration region are shown in Figure 13 for various binary separations. The uppermost curve corresponds to the combined acceleration and convection region π^0-decay spectrum for a binary separation of $D = 10^{14}$ cm.

For typical parameters of colliding massive wind systems and maximal allowed injection power, the radiative luminosity from π^0-decay lies therefore typically on a level $\le 10^{33}$ ergs s^{-1}, leading to a π^0-decay luminosity from wide binary systems that can in general be neglected when compared to the expected IC luminosity above 1 GeV, provided the emitting electron spectrum extends to $\ge 10^4$ MeV.

4.4. γ-γ Opacity in the Stellar Radiation Fields

Above ~100 GeV the optical depth $\tau_{\gamma\gamma}$ due to photon-photon pair production ($\gamma\gamma \rightarrow e^+ e^-$) in the intense stellar radiation field of the main-sequence star may reach nonnegligible values depending on its spectral type. This may modify the γ-ray spectrum escaping from the source by a factor $\exp(-\tau_{\gamma\gamma})$.

The γ-γ opacity $d\tau_{\gamma\gamma}$ along a path element dy in a radiation field with differential photon number density $n(\epsilon, \Omega)$ is given by (Gould & Schreder 1967)

$$d\tau_{\gamma\gamma}(E_\gamma, \epsilon, \Omega) = dy \, d\epsilon \, d\Omega \, n(\epsilon, \Omega) \sigma_{\gamma\gamma}(\epsilon, E_\gamma, \mu_{\gamma\gamma})(1 - \mu_{\gamma\gamma}), \tag{30}$$

where $\mu_{\gamma\gamma}(y) = \cos\theta_{\gamma\gamma}(y)$ is the cosine of the angle between the two interacting photons. For photons of energy E_γ escaping from the emission region at location r along a path y with angle

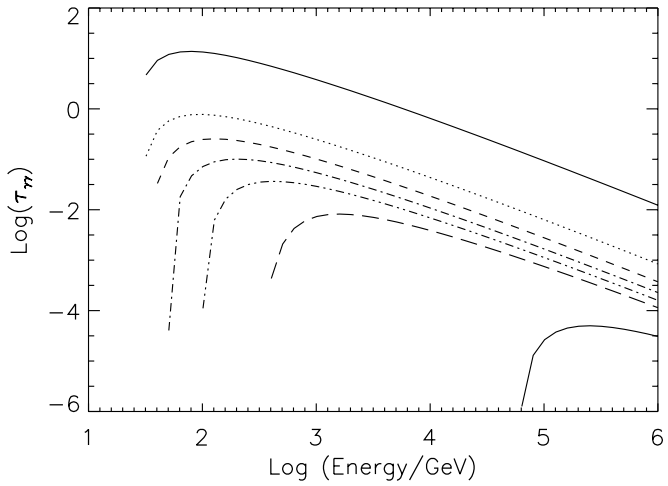

FIG. 14.—The $\gamma\gamma$ pair production opacity $\tau_{\gamma\gamma}$ for a binary separation of $D = 10^{14}$ cm and for angles $\theta_L = 0^\circ$ (*lower solid line*), 30° (*long-dashed line*), 60° (*double-dot–dashed line*), 90° (*dash-dotted line*), 120° (*dashed line*), 150° (*dotted line*), and 180° (*upper solid line*), and fixing r at 10^{12} cm.

$\mu_{\rm ph} = \cos\theta_L \cos\theta + \sin\theta_L \sin\theta \cos(\phi - \phi_L)$, the target photon density above the stellar radius r_s is

$$n(\epsilon, \Omega) = n_0 \, \frac{4\pi r_s^2}{\tilde{x} + y^2 + 2y\mu_{\rm ph}\sqrt{\tilde{x}}} \delta(\epsilon - \epsilon_T)\delta(\mu - \mu_{\gamma\gamma})\delta(\phi),$$

where $\tilde{x} = x^2 + r^2$. This can be rewritten as

$$\tau_{\gamma\gamma}(E_\gamma, \mu_{\rm ph}, x, r) = n_0 r_s^2 \int_0^\infty dy \, \frac{(1 - \mu_{\gamma\gamma})\sigma_{\gamma\gamma}(s)H(s - s_{\rm thr})}{\tilde{x} + y^2 + 2\sqrt{\tilde{x}}y\mu_{\rm ph}}. \quad (31)$$

Here, $s = 2E_\gamma\epsilon[1 - \mu_{\gamma\gamma}(y)]$ is the square of the center of momentum (CM) energy, $\sigma_{\gamma\gamma}(s)$ is the cross section for photon-photon pair production (Gould & Schreder 1967), and $s_{\rm thr} = (2m_e c^2)^2$ is the squared minimum CM energy.

In Figures 14–16 we show the absorption optical depth due to photon-photon collisions in a $T = 43{,}000$ K radiation field (i.e., $\epsilon_T = 10$ eV) for different $r_{\rm OB} = (1.2\text{–}24) \times 10^{13}$ cm, being the separation of the emission region from the stellar photosphere, and for various angles $\theta_L = 0^\circ\text{–}180^\circ$, respectively. Large viewing angles decrease the process' threshold energy in the observer frame and increase the opacity at the same time due to a longer pathway and the rise of the CM energy. Figure 14 shows that variations of the optical depth with angle θ_L by several orders of magnitude are possible, and absorption can be quite severe (up to $\tau_{\gamma\gamma} \sim 100$ for $D = 10^{14}$ cm). Except at large θ_L the effect of varying r mainly impacts the absorption depth near threshold (see Fig. 15). The opacity is also strongly dependent on the radiation field density, which is dependent on the massive star's luminosity, as well as on $r_{\rm OB}$. This can be observed in Figure 16, where $\tau_{\gamma\gamma}$ ranges between 0.002 to 0.04 at the peak of the cross section and along the $\theta_L = 45^\circ$ sight line.

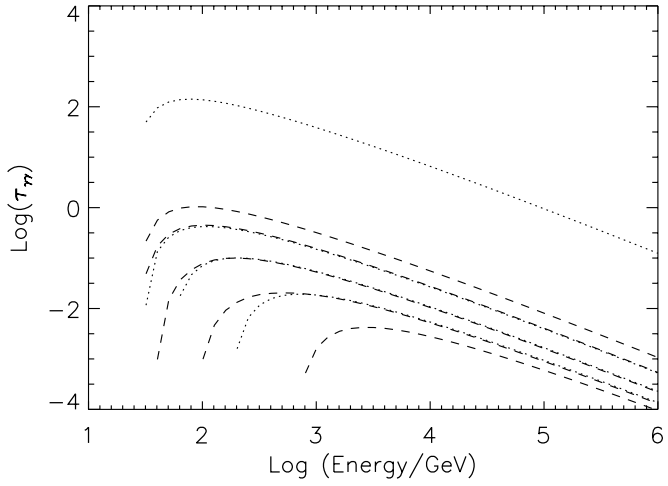

FIG. 15.—The $\gamma\gamma$ pair production opacity $\tau_{\gamma\gamma}$ for a binary separation of $D = 10^{14}$ cm and varying $r = 10^{11}$ cm (*dotted lines*) and 10^{13} cm (*dashed lines*), and for angles $\theta_L = 0^\circ$, 45°, 90°, 135°, and 180° (*from lower to upper curves*).

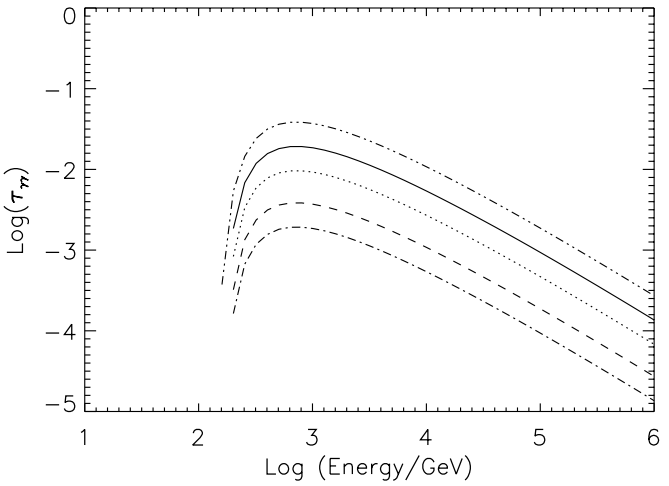

FIG. 16.—The $\gamma\gamma$ pair production opacity $\tau_{\gamma\gamma}$ for an angle of $\theta_L = 45^\circ$ and for a separation between the collision region and the OB star surface of $r_{\rm OB} = 2.4 \times 10^{14}$ cm (*dash-dotted line*), 1.2×10^{14} cm (*dashed line*), 4.8×10^{13} cm (*dotted line*), 2.4×10^{13} cm (*solid line*), and 1.2×10^{13} cm (*double-dot–dashed line*) and fixing r at 10^{12} cm.

This essay shows that γ-ray absorption due to pair production cannot be neglected in general for massive star systems but must be treated individually for each system, with a strong dependence of the line of sight. If the pair production happens near threshold and the optical depth is not very large, then the resulting electron-positron pair is only mildly relativistic and has little impact on the observed emission. One should note that most pairs would be produced outside of the acceleration zone, so they would not be accelerated and a pair cascade would not develop, in contrast to the situation in, e.g., the magnetosphere of a pulsar.

5. APPLICATIONS

5.1. *WR 140*

WR 140 is the archetype of a spectroscopic long-period massive binary system of colliding winds that shows periodic dust formation around periastron passage, as well as nonthermal radio emission at phases in which the colliding wind region is outside the photosphere for free-free absorption. The system has been well monitored at radio, infrared (IR), optical, UV, and X-rays (e.g., Williams et al. 1990; White & Becker 1995; Panov et al. 2000; Setia Gunawan et al. 2001b). It consists of a WC 7pd and a O4–5 V companion (of bolometric luminosity $L_{\rm bol} = 10^{6.18}\ L_\odot$ and effective temperature $T_{\rm eff} = 47{,}400$ K) with an orbital period of 2899 ± 10 days. Located at a distance of 1.85 kpc (Dougherty et al. 2005) the large-inclination system

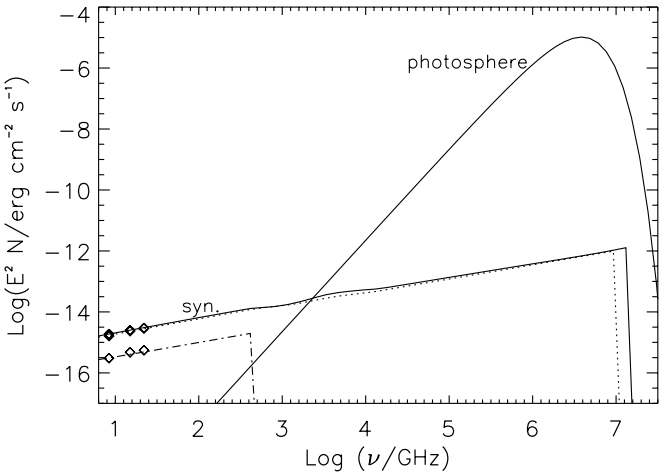

FIG. 17.—Synchrotron spectra for WR 140 at phases 0.955 (*dash-dotted line*), 0.671 (*dotted line*), and 0.8 (*lower solid line*) from electron spectra as shown in Fig. 17 and using the δ-approximation in comparison to the observed nonthermal radio emission taken from Dougherty et al. (2005). Below $\sim$8 GHz the radio flux is likely dominated by absorption effects. The bulk of the synchrotron component is hidden below the photospheric UV radiation from the O star. The thermal X-ray emission from the hot shocked gas in the collision region is not shown here.

($i = 122^\circ \pm 5^\circ$; Dougherty et al. 2005) possesses an eccentricity of 0.881 ± 0.04. With periastron passage being defined by phase $\Phi = 0$, the argument of periastron is $\omega = 47^\circ$ (Marchenko et al. 2003). In this work we use the basic parameters that have been recently redetermined by Dougherty et al. (2005). The mass-loss rate of $8.7 \times 10^{-6}\ M_\odot\ \mathrm{yr}^{-1}$ and the wind velocity of the O star $v_{\mathrm{OB}} = 3100\ \mathrm{km\ s}^{-1}$, as compared to the mass-loss rate of $4.3 \times 10^{-5}\ M_\odot\ \mathrm{yr}^{-1}$ of the WR star at velocity $v_{\mathrm{WR}} = 2860\ \mathrm{km\ s}^{-1}$, places the collision region at a distance of $x \approx 0.32D \approx 9.6 \times 10^{12}$–$1.5 \times 10^{14}$ cm from the O star, depending on the orbital phase of the system. This is a factor of $\sim$2.5 smaller than that used in earlier works (e.g., Eichler & Usov 1993; Benaglia & Romero 2003). At this distance the wind gas density lies between $\sim 4 \times 10^6$–$9 \times 10^8\ \mathrm{cm}^{-3}$. For the strength of the shock we assume a compression factor $c_r = 4$. The radio emission comprises a thermal bremsstrahlung and a nonthermal synchrotron

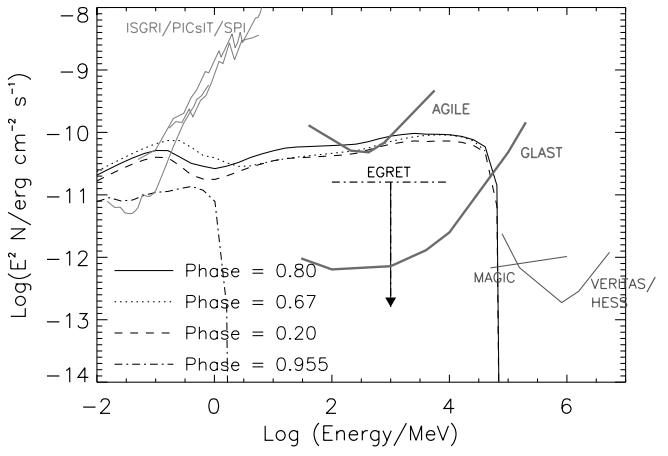

FIG. 18.—IC spectra for WR 140 at phases 0.955, 0.2, 0.671, and 0.8 from electron spectra as shown in Fig. 17. The spectral changes from γ-ray absorption are not shown here. The EGRET 2 σ upper limit (Mücke & Pohl 2002) is based on observations that correspond to a superposition of orbital states rather determined by periastron phase and should therefore apply to phase 0.955. [*See the electronic edition of the Journal for a color version of this figure.*]

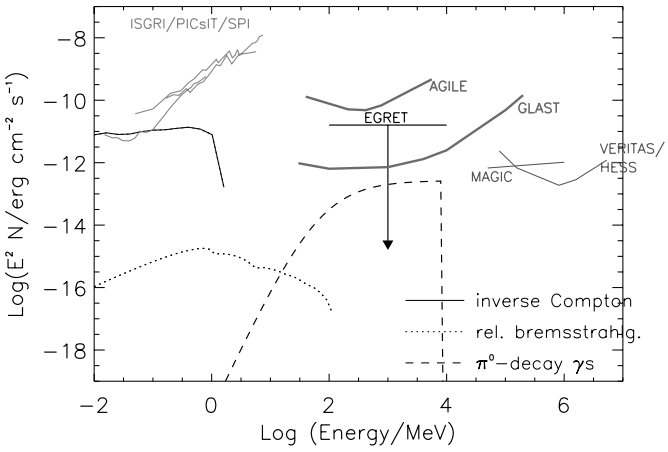

FIG. 19.—Broadband SED of WR 140 at orbital phase 0.955 (close to periastron). The injected energy in electrons and protons is equal and $\sim 10^{-5}$ times the kinetic OB wind energy. See text for further parameters and discussion. The γ-ray absorption alters the spectrum significantly only above $\sim$60 GeV. The escaping photon spectrum remains therefore unchanged at this orbital phase. [*See the electronic edition of the Journal for a color version of this figure.*]

component and reaches its maximum roughly at phase 0.83. The nonthermal radio emission at phases $\Phi = 0.671$–0.955 shows typically a $\alpha = -0.5$ spectrum, indicating that the underlying particle distribution obeys a power law with spectral index $p = 2$ (Williams et al. 1990; Dougherty et al. 2005). The spectral shape of the nonthermal component can be used to place constraints on the diffusion coefficient in the framework of our simplified geometric model if the compression ratio and convection velocity are known (see § 3). The spectral requirements are in agreement with a convection velocity of $\sim$1500 km s^{-1}, a compression ratio $c_r = 4$, and $\kappa_a = 4\kappa_d$. The observed synchrotron radio spectrum places severe limits on the underlying electron distribution and hence constrains the high-energy emission. For predicting WR 140's γ-ray emission from primary electrons and protons, we have selected four orbital phases for which its nonthermal radio emission has been determined (Dougherty et al. 2005), namely, $\Phi = 0.995$, 0.2, 0.671, and 0.8. In order to reproduce the flux level of the centimeter radio data for those phases (see Fig. 17), we require a energy injection rate of thermal particles that varies with orbital phase and lies between $10^{32.5}$ and $10^{33.5}$ ergs s^{-1} or 10^{-3}% to 10^{-2}% of the OB wind kinetic energy. The total emission volume $V = r_{\mathrm{max}}^2 \pi d$, with $d \sim x$, is also assumed to vary with orbital phase (we used $r_{\mathrm{max}} = 4 \times 10^{14}$ cm for $\Phi = 0.2$, 0.671, and 0.8, and $r_{\mathrm{max}} = 10^{13}$ cm for $\Phi = 0.995$), as suggested by the centimeter radio observations (Dougherty et al. 2005). The magnetic field at the O star surface is assumed of order 100 G, which leads to field values of 0.2–3.5 G in the wind collision zone (in agreement with estimates for the equipartition magnetic field; Benaglia & Romero 2003). The diffusion coefficient κ_a determines the acceleration rate and, together with the energy loss channels, the maximum particle energy. In order to allow for relativistic electron energies, necessary to explain the observed synchrotron radiation, κ_a must be low enough that acceleration gains are able to overcome the Coulomb losses. On the other side, Bohm diffusion is the limit for the diffusion coefficient κ_d, which is connected to κ_a. This leads to a rather narrow range of possible values for the diffusion coefficients compatible with the production of >100 MeV photons via the IC process at least at phases close to apastron. For our models presented in Figures 18–20, we used $\kappa_a = 3.76 \times 10^{19}\ \mathrm{cm}^2\ \mathrm{s}^{-1}$, which results in an acceleration region size of $r_0 = (2.4$–$2.6) \times 10^{11}$ cm and an

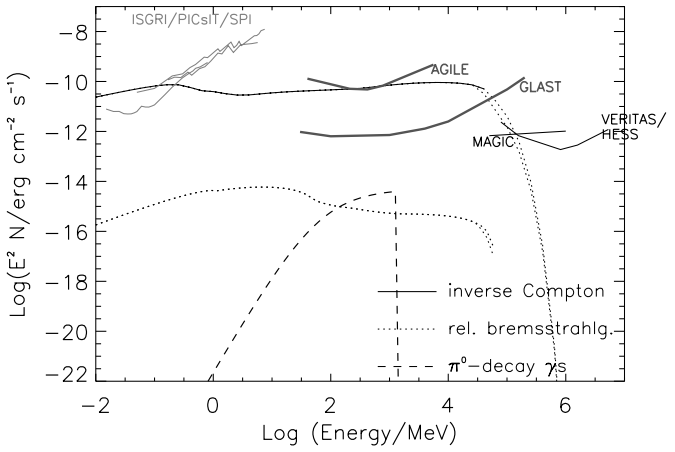

FIG. 20.—Broadband SED of WR 140 at orbital phase 0.671. An injected electron energy of 3×10^{33} ergs s^{-1} in total are required to account for the synchrotron flux at this phase. For the protons we used $Q_0 E_{0,\mathrm{kin}} \sim 8 \times 10^{-7} L_w$ ($E_{0,\mathrm{kin}} = 1$ MeV). See text for further parameters and discussion. The γ-ray absorption due to photon collisions in the radiation field of the OB star has been taken into account for all radiation processes: IC (*solid line*), bremsstrahlung (*dotted lines*), and π^0-decay γ-rays (*dashed line*). The corresponding upper and lower curves belong to the unabsorbed and absorbed fluxes, respectively. The cutoff in the IC spectrum has been extended (*dotted line*) using an exponential shape to guide the reader's eye. See text for details. [*See the electronic edition of the Journal for a color version of this figure.*]

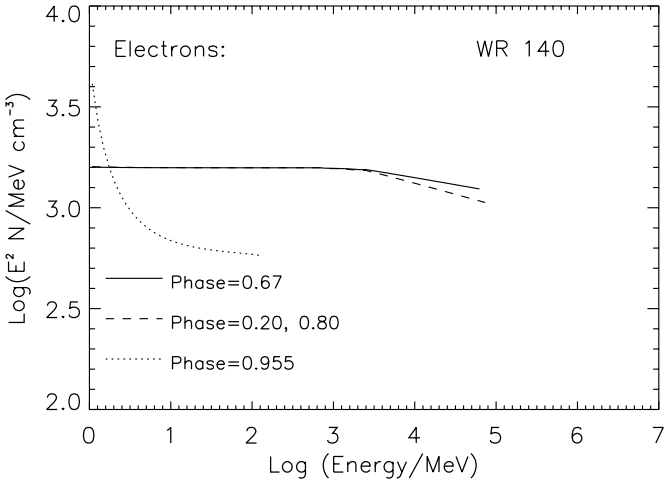

FIG. 21.—Steady state electron spectra for WR 140 at orbital phases 0.955, 0.2, 0.671, and 0.8, with $Q_0 = 1$. See text for parameters and discussion.

escape time of $T_0 = 1.6$–1.9 ks. Observational indications of the maximum photon energy will shed light on the exact value of κ_a.

Figure 21 shows the steady state electron spectra at orbital phases 0.955 (close to periastron), 0.2, 0.671 (close to apastron), and 0.8 for these parameter values. The wind collision region is located closest to the main-sequence star at periastron, while it is farthest away at apastron. All spectra except at periastron extend to very high energies with the cutoff due to the finite size of the acceleration region and a smooth change in the spectral index where Klein-Nishina effects set in. The sharpness of the cutoff is a result of the approximations employed in this work and may appear somewhat softened in more sophisticated (however, then indispensably nonanalytical) calculations.

With these parameters the synchrotron spectrum does not extend beyond the extreme UV range (see Fig. 17), which is heavily dominated by the photospheric emission of the hot O star. The IR energy band is affected by thermal radiation from episodic dust formation (e.g., Williams et al. 1990). The overwhelming part of the X-ray band is dominated by thermal X-ray emission from the collision region (e.g., Williams et al. 1990; Stevens et al. 1992). This significantly complicates the extraction of any nonthermal X-ray component, which would provide valuable information about the electron distribution at energies that potentially determine the γ-ray output. Given the limitations in the achievable electron energy, any nonthermal component emerging in the hard X-ray band is likely due to IC scattering.

At periastron the wind collision region is closest to the OB star, and the electron spectrum is cut off already at $\sim$100 MeV due to (Thomson regime) IC losses in the intense photospheric radiation field. Figures 19 and 20 show the corresponding broadband spectral energy distributions (SEDs) in comparison with the sensitivity of the *INTEGRAL* instruments, *GLAST*, AGILE and the current generation IACTs like High Energy Stereoscopic System (HESS), Major Atmospheric Gamma Imaging Cherenkov (MAGIC) telescope, and VERITAS. The EGRET upper limit has been derived from the summed P1–P4 EGRET data at the location of WR 140 (see also Mücke & Pohl 2002). At all orbital phases IC emission dominates over all other radiation processes except close to periastron. Here the IC spectrum cuts off already at a few MeV, corresponding to the cutoff in the electron spectrum. The γ-ray domain is therefore only covered by relativistic bremsstrahlung radiation (up to $\sim$100 MeV following the electron spectrum) and γ-rays from the π^0-decay. The (ion-electron) bremsstrahlung emission turns out to lie always below the IC photon output at a level that is not detectable for current and near-future instruments. Assuming the maximal possible injection rate of thermal particles into the acceleration region, π^0-decay γ-rays may possibly be detected with *GLAST* at orbital phases close to periastron where the density of the target material is enhanced. At apastron the losses in the photospheric radiation field, as well as due to the wind particle density are low enough to allow the photon spectra to extend into the 10–100 GeV regime with a detectable IC flux level, particularly with low-energy threshold IACTs (e.g., MAGIC) and *GLAST*. This is true despite photon absorption from pair production, which leaves its fingerprint above $\sim$100 GeV [see Fig. 20: at $\Phi = 0.67$, $\tau_{\gamma\gamma}(r = r_0, E \approx 100\ \mathrm{GeV}) \sim 1$, while at $\Phi = 0.95$, $\tau_{\gamma\gamma}(r = r_0, E \approx 100\ \mathrm{GeV}) \sim 3$].

Figure 18 zooms into the IC spectra. The flux variations due to the anisotropy effect at different orbital phases are blurred by flux variations due to the changes in the radiation field density in the strongly eccentric system. The feature at $\leq$1 MeV stems from the deficit of high-energy particles in the convection zone. For this parameter setting we predict a maximum of the IC flux at phase $\Phi \simeq 0.95$, the minimum IC flux level would occur at phase $\sim$0.01. Thus, the next maximum γ-ray flux level is expected around 2008 August, well in time for an observation with *GLAST*.

5.2. *WR 147*

WR 147, a WN8(h) plus B0.5 V (with bolometric luminosity of $L_{\mathrm{bol}} = 5 \times 10^4\ L_\odot$ and effective temperature $T_{\mathrm{eff}} = 28{,}500$ K, i.e., $\epsilon_T \approx 6.6$ eV) binary system is among the closest and brightest systems that show nonthermal radio emission in the centimeter band. Owing to its proximity, this system has been resolved in a northern nonthermal component (WR 147N) and a southern thermal one (WR 147S) with a separation of 575 ± 15 mas using the MERLIN instrument (Churchwell et al. 1992; Williams et al. 1997). The observed radio morphology and spectrum supports a colliding wind scenario for WR 147, as first proposed by Williams

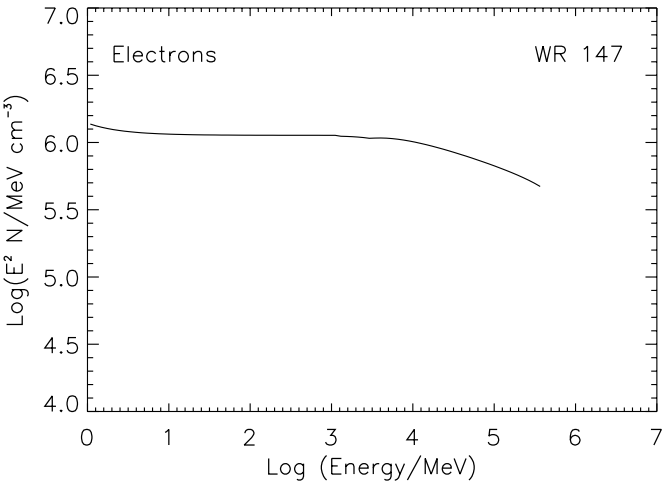

FIG. 22.—Steady state electron spectrum for WR 147, with $Q_0 = 1$. See text for parameters and discussion.

et al. (1997). At a distance of 650 pc the implied binary separation is estimated to be 417 AU. The mass-loss rates ($\dot{M}_{\rm WR} = 2.5 \times 10^{-5}\,M_\odot\,{\rm yr}^{-1}$, $\dot{M}_{\rm OB} = 4 \times 10^{-7}\,M_\odot\,{\rm yr}^{-1}$) and wind velocities ($v_{\rm WR} = 950\,{\rm km\,s}^{-1}$, $v_{\rm OB} = 800\,{\rm km\,s}^{-1}$) place the stagnation point at 6.6×10^{14} cm, in agreement with the MERLIN observations. A comprehensive study of WR 147's radio emission and the geometry of the system has been presented by Setia Gunawan et al. (2001a). Neither the eccentricity nor the inclination of the system are known so far; hence, we assume $i = 90^\circ$ and $e = 0$ for this application to WR 147. The nonthermal flux component can be well fitted by a power law with spectral index $\alpha = -0.43$, with, however, poor statistical significance. The spectral shape and flux level of this synchrotron component is again used to set constraints on the acceleration parameters and overall nonthermal particle content in WR 147's wind collision region. Here we use again the canonical value of $\alpha = -0.5$ corresponding to an E^{-2} power-law particle spectrum. Assuming strong shocks, a convection velocity of $\sim$400 km s^{-1} and a B star surface magnetic field of 30 G (translating into a 25 mG field strength in the wind collision region, close to its equipartition value; Benaglia

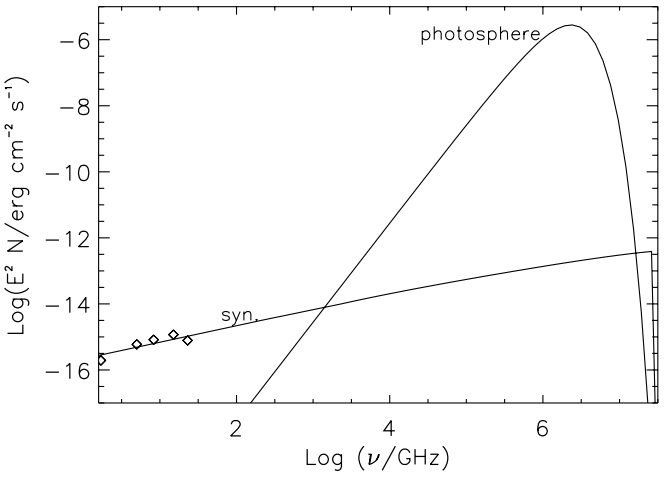

FIG. 23.—Synchrotron spectra for WR 147 from electron spectra as shown in Fig. 22 and using the δ-approximation in comparison to the observed nonthermal radio emission taken from Setia Gunawan (2001a). The bulk of the synchrotron component is hidden below the photospheric UV radiation from the B star. The thermal X-ray emission from the hot shocked gas in the collision region is not shown here.

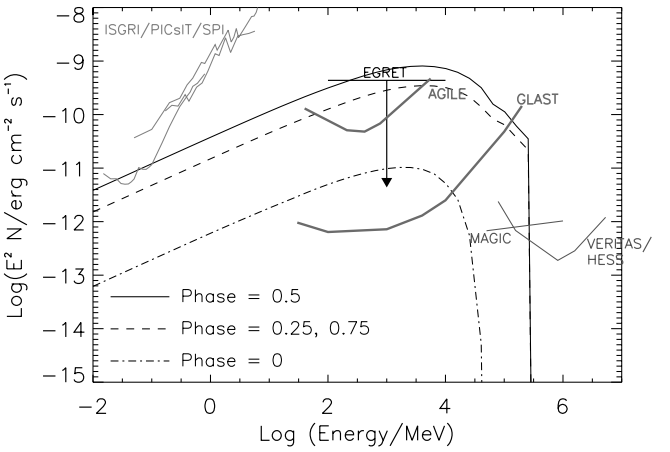

FIG. 24.—IC spectra of WR 147 for orbital phases 0, 0.25, 0.5, and 0.75 for an underlying electron spectrum as shown in Fig. 22, neglecting any eccentricity of the system and assuming $i = 90^\circ$. The EGRET upper limit, estimated by Benaglia & Romero (2003), may not be fully applicable here due to the 4 year averaging of the data. See text for further parameters and discussion. The $\gamma\gamma$ pair production absorbs not more than $\leq$0.3% (>50 GeV) and $\leq$18% (>100 GeV) of the produced flux at orbital phases 0.25 and 0.5, respectively (not shown in figure). No absorption takes place at phase 0. [*See the electronic edition of the Journal for a color version of this figure.*]

& Romero 2003), the observed radio flux level can be reproduced if $\sim$0.15% of the OB wind kinetic energy is available for particle acceleration in an emission region of a total estimated volume of $\sim 2.6 \times 10^5\,{\rm AU}^3$ (see Fig. 23). Again, the value for the diffusion coefficient must be low enough to allow acceleration to overcome the Coulomb losses, since relativistic particles are observed to exist. Similarly, the Bohm limit shall not be violated. The remaining freedom of choice in the diffusion coefficient's value is used to represent typical production of high-energy γ-rays through the IC process. With $\kappa_a = 2 \times 10^{21}\,{\rm cm}^2\,{\rm s}^{-1}$, convection is dominant in $\sim$90% of the total emission region, and the acceleration site covers a size of $r_0 = 5 \times 10^{13}$ cm (escape time is $T_0 \approx 10^6$ s).

In Figure 22 the resulting steady state electron spectrum is shown. For a negligible system eccentricity, it is the same at all orbital phases. The steepening at 10^4–10^5 MeV is due to synchrotron losses, and the slight upturn toward lower energies reflects the influence of the Coulomb losses. Above $\sim 10^{5.5}$ MeV the Bohm limit cuts off the particle spectrum. The resulting synchrotron spectrum is mostly hidden below the strong photospheric emission from the B star (see Fig. 23) and the thermal X-ray component from the shock-heated wind collision region (Setia Gunawan et al. 2001a). At higher energies IC emission likely dominates the radiative energy output. Figure 24 demonstrates the orbital IC flux variations due to the anisotropic nature of the IC scattering of more than 1 order of magnitude for the chosen system inclination. The maximum flux level is expected when the WR star is behind the OB star along the sight line. These flux changes will be, in principle, detectable for *GLAST* at all orbital phases and also for low-threshold IACTs, provided sufficiently high particle energies are reached, which by itself depends on the acceleration rate. Thus, measurements with IACTs will be able to place sensitive constraints on the acceleration efficiency in these environments. The EGRET upper limit estimate is taken from Benaglia & Romero (2003). For a wind gas density of up to 1.4×10^5 cm^{-3}, nonthermal bremsstrahlung emission remains several orders of magnitude below the IC flux level and thus not detectable with current instrumentation. Also, the contribution from π^0-decay γ-rays remains negligible, even for a maximum possible

thermal particle injection rate. For WR 147, being an extremely long-period binary with a presumably small eccentricity, the photospheric UV radiation field at the location of the collision region is low enough to allow here the neglect of γ-ray absorption due to photon-photon collisions.

6. DETECTABILITY FROM SOFT TO VERY HIGH ENERGY GAMMA-RAYS

6.1. *Soft Gamma-Ray Instruments*

The regime of soft γ-rays, here considered to be typical ranging from 511 keV up to several MeV, is currently only accessible by the IBIS and SPI instruments on board *INTEGRAL*. Previous mission like *GRANAT* SIGMA and COMPTEL did not report the detection of soft γ-ray emission from the WR binary systems studied here. Given the continuum sensitivity of the IBIS and SPI instruments,[4] accordingly scaled for a common observation time of 10^6 s in order to achieve a 3 σ detection, the detection of WR 140 appears to be possible at soft γ-rays only if significantly more observation time than 1 Ms will be dedicated to observations toward such an object. Hard X-ray emission may be seen by ISGRI, most favorably in orbital phases when the line of sight toward an observer is parallel to the contact discontinuity of the wind collision zone or when both the WR and O star are nearly aligned and the wind collision zone is most pronouncedly exposed toward the observer. At soft γ-rays, even in the most favorable orbital states, several megaseconds may be required to pick up emission from WR 140 (Fig. 18). This situation is very similar for WR 147 (Fig. 24).

6.2. *High-Energy Gamma-Ray Instruments*

At energies between 30 MeV and 10 GeV, detection claims of γ-ray emission from WR binary systems have been made already from *Cosmic-Ray Satellite B* (*COS-B*) observations. More particular, WR 140 (HD 193793) was considered to be associated with the variable *COS-B* source 083+03 (Pollock 1987), a source exhibiting a photon flux at the 5×10^{-7} photons cm^{-2} s^{-1} level at $E > 300$ MeV. However, this individual association could not be confirmed by observations of the EGRET instrument on board the *Compton Gamma-Ray Observatory* (*CGRO*), which would have seen a source at $\sim 1.5 \times 10^{-6}$ photons cm^{-2} s^{-1} at $E > 100$ MeV. Although a number of positional coincidences between unidentified EGRET sources and CWB systems has been noted by Kaul & Mitra (1997) and Romero et al. (1999), the individual case for an association between WR 140 and the unidentified EGRET source 3EG J2022+4317 appears to be vague on the basis of the given observational evidence at γ-rays. The source 3EG J2022+4317 is cataloged (Hartman et al. 1999) with a flux of 2.5×10^{-7} photons cm^{-2} s^{-1}, and the spectrum is fitted with a power law with an index of 2.3 ± 0.2; it is further characterized by a rather irregular source location uncertainty contour pointing toward source extension, and an indication of source confusion above $E > 100$ MeV. The EGRET observations were taken within the first 4 years of the *CGRO* mission between 1991 and 1994, with most observations obtained toward the periastron phase of the binary system. In the sparse EGRET detections above the 3EG catalog threshold, there is no evidence for variable γ-ray emission (Nolan et al. 2003). Since WR 140 is at a distance of $0\overset{\circ}{.}67$ to the nominal position of 3EG J2022+4317, and only barely consistent with the 99% source location uncertainty contour, which prevents any conclusive association between both objects, it is appropriate to determine an upper limit at the position of WR 140 under consideration that γ-ray emission of 3EG J2022+4317 is fully taken into account but not been associated with WR 140 (Mücke & Pohl 2002). This upper limit is consistent with our predictions given in Figure 18, considering that EGRET observations were performed over a superposition of orbital states including the periastron phase, where the cutoff due to IC losses in the Thomson regime will not allow any detectable γ-ray emission at all at energies above a few MeV. Since AGILE will exhibit a similar sensitivity characteristics compared to the EGRET instrument, chances for AGILE to clarify the nature of 3EG J2022+4317 are only available if AGILE is operated in orbit over a long period. The instrumental sensitivity of AGILE[5] is indicated for a 5 σ detection on the basis of 10^6 s observation time. Thus, *GLAST* will give an observational reassessment of the unidentified EGRET source 3EG J2022+4317 and its association or nonassociation with WR 140. Clearly, *GLAST*[6] not only has the sensitivity characteristics to achieve a detection from observations accumulated over various orbital states of the CWB; it also has a privileged chance to provide results from individually selected orbital states. As mentioned above, during periastron phase there is no high-energy γ-ray emission predicted (Fig. 19), but the variations in the γ-ray flux of WR 140 when going into periastron or coming out of periastron phase will be detectable, since the sensitivity of *GLAST* will be indeed sufficient to detect this system in the more favorable orbital states either when the edges of the contact discontinuity of the wind collision zone lines up in the line of sight or the wind collision zone is most extensively exposed toward the observer. *GLAST* will have this detection potential up to energies at which the finite acceleration site cuts off the emission, approximately up to $\sim$50 GeV. The chance to detect high-energy emission in case of WR 147 with future instruments is even somewhat better than for WR 140. If AGILE with its better instrumental point-spread function than EGRET will be able to distinguish the location of WR 147 from the bright γ-ray source 3EG J2033+4118, its sensitivity will be sufficient to observe γ-ray emission over the majority of favorable orbital states (Fig. 24). However, the periastron phase will still be out of reach for AGILE; see Figure 25.

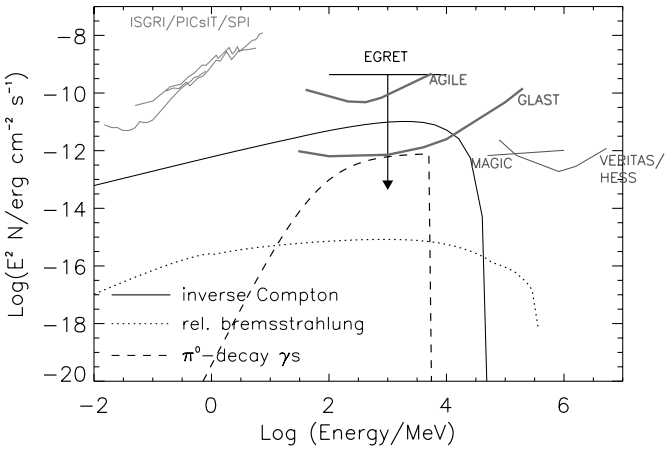

FIG. 25.—Broadband SED of WR 147 at orbital phase 0. See text and Fig. 24 for further parameters and discussion. [*See the electronic edition of the Journal for a color version of this figure*.]

[4] See INTEGRAL AO-3 Documentation at http://www.rssd.esa.int/Integral/AO3/.

[5] See http://agile.rm.iasf.cnr.it/a-sens.html.

[6] See http://www-glast.slac.stanford.edu/software/IS/glast_lat_performance.htm.

GLAST, again, will have the instrumental capability to both distinguish a test position at the location of WR 147 ($l = 79.^{\circ}85$, $b = -0.^{\circ}32$) from the presumably bright γ-ray source 3EG J2033+4118. Depending on a possible contribution from further subthreshold sources in the vicinity of 3EG J20233+4118, this might not be too straightforward, however.

6.3. *Very High Energy Gamma-Ray Instruments*

Energetically complementary to the satellite experiments operated at soft and high-energy γ-rays, the continuous development of IACTs toward better sensitivity, even more improved angular resolution, and lower energetic thresholds enables ground-based γ-ray experiments to detect γ-ray emission produced in colliding winds of massive stars in binary systems. In particular, the chance to accumulate a wealth of photons on subhour timescales will enable the IACTs to test the predicted orbital flux variations precisely. A unique chance to detect emission from WR 140 is given for those experiments promised to work at the lowest possible threshold, i.e., MAGIC below 100 GeV. Depending on the actual shape of the cutoff due to the finite site of the acceleration site, events may be seen only in extreme low energy event selections, and the respective sky location is further characterized by an absence of higher energy photons. For an array of IACTs like VERITAS (Weekes et al. 2002) the best sensitivity is achieved at energies above the cutoff due to the finite acceleration site in WR 140, subsequently making any detection prospects heavily dependent on the actual shape of the cutoff. IACT arrays located in the southern hemisphere like HESS or CANGAROO may not have the chance to detect this system at all due to the higher energetic threshold when observing under low zenith angle conditions. In the case of WR 147, in which the orbital parameters are more promising for detecting high-energy γ-ray emission up to several hundred GeV, low-threshold IACTs located in the northern hemisphere will have a distinct chance to detect WR 147 in nonperiastron orbital phases (Fig. 24), provided that the γ-ray analysis will not introduce quality cuts for preference of a higher energy event selection. For both satellite and ground-based instruments, the colliding wind zone will not appear to be spatially resolved, presenting individual CWB systems as point-source candidates at the γ-ray sky.

7. CONCLUSIONS AND DISCUSSION

In this work we have calculated the emission from nonthermal steady state particle spectra built up in the regions of colliding hypersonic winds (assumed to be homogeneous) of long-period massive binary systems with the stagnation point defined by balancing the wind momenta and under the assumption of spherical winds. The shocked high-speed winds are creating a region of hot gas that is separated by a contact discontinuity. The gas flow in this region away from the stagnation point will be some fraction of the wind velocity, which we kept constant here. A simplification of the geometry from a bow-shaped to a cylinder-shaped collision region allowed us to solve the relevant diffusion loss equations analytically. We considered first-order Fermi acceleration out of a pool of thermal particles and took into account radiative losses (synchrotron, IC including Klein-Nishina effects, bremsstrahlung, and Coulomb losses) and (energy-independent) diffusion by introducing a constant escape time T_0 and convection/advection with constant speed. Above a certain distance from the stagnation point, convection dominates over diffusion, with the transition point determined by balancing the diffusion and convection loss time. Correspondingly, we divided the emission region into a region where acceleration/diffusion dominates, the "acceleration zone," and the outer region where convection/advection dominates, the "convection zone."

Electrons may reach relativistic energies once they overcome the heavy Coulomb losses in the dense shocked material, through diffusive shock acceleration up to the Bohm diffusion limit. For wide binary systems this latter constraint is often severe, while for close binaries, radiative losses mostly cause the cutoff. Generally, we find that the electron spectrum cuts off at energies that do not permit significant multi-TeV γ-ray emission, in contrast to the X-ray binary LS 5039 (Aharonian et al. 2005b) and the binary system PSR 1259−63/SS 2883 (Aharonian et al. 2005a), from which TeV-scale emission has been observed recently. We have not considered an increase of the cutoff energy as caused by a runaway streaming instability in the acceleration region, which would amplify the magnetic field and hence reduce the Bohm diffusion coefficient (Lucek & Bell 2000; Bell & Lucek 2001).

Taking into account existing upper limits of the stellar surface magnetic field strength of massive stars, IC losses in general dominate over synchrotron losses if in the Thomson loss regime. We have shown, however, that losses may well extend into the transition region leading to the extreme Klein-Nishina regime. The flattening of the Compton loss rate there may in some cases cause the synchrotron losses to dominate eventually. *Thus, a rigorous treatment of the Compton losses shall include Klein-Nishina effects.* For this purpose we have derived analytical approximations for Klein-Nishina losses that are suitable for massive binary systems and at the same time have solved the relevant diffusion loss equation analytically. Despite the high-density environment of the emitting collision region, nonthermal bremsstrahlung losses generally prove to be of minor importance. This turns out to be true also for the corresponding radiation.

We have studied IC radiation, the main emission channel for relativistic electrons in these systems, in full detail. The use of the full Klein-Nishina cross section leads to a spectral softening at the high-energy end of the emitted radiation. Since the stellar target photons for IC scattering arrive at the collision region from a preferred direction, the full angular dependence of the scattering process has to be considered. Its anisotropic nature leads to variations of the flux level by up to several orders of magnitude (depending on system inclination and eccentricity), as well as cutoff energy with orbital phase. The maximum flux and cutoff energy occurs when the WR star lies behind the OB star. We consider therefore massive binary systems as γ-ray sources that are variable on the timescale of their orbital period even in the absence of a strong system eccentricity. The inclusion of convection/advection effects into the calculation of the particle spectra also reveals a possibly visible spectral feature. Because of a deficit of low-energy particles in the convection zone, a softening of the volume-integrated radiation spectrum may occur if the convection zone is sufficiently large compared to the acceleration zone. A detection of such features would give information about the particle propagation properties in the emission region.

Since thermal protons are most likely wind constituents as well, diffusive shock acceleration implies the presence of relativistic protons in the wind collision region. If they reach energies of several GeV, their presence may show up as π^0-decay γ-rays produced through inelastic proton-proton collisions. Their detectability, however, depends not only on the relativistic electron-to-proton ratio and the instrument capabilities, but also on the importance of the competing radiation mechanisms. For example, in the case of WR 140 close to periastron, the otherwise dominant IC radiation most likely ceases to reach sufficiently high energies that would allow MeV–GeV emission, which increases the chance of detecting π^0-decay γ-rays.

Finally, we find that photon-photon pair production cannot be neglected if the produced radiation exceeds energies of $\sim(kT/\mathrm{eV})^{-1}$ TeV, which lies typically at 50–100 GeV. The absorption optical depth thereby depends sensitively on orbital phase and system inclination.

The basic assumptions of our model are a simplified cylinder-like geometry of the colliding wind region; that the stellar winds are spherical, uniform and homogeneous; a simplified behavior of the convection velocity; and the energy-independence of the diffusion coefficients, together with the leaky box treatment of the acceleration region (which allows the spatial decoupling of diffusion and convection), with acceleration assumed to operate through the well-established diffusive shock acceleration. For a given surface magnetic field strength, the field value at the colliding wind region, assumed to be constant within the emission region, is estimated through the conventional stellar outflow topology (Weber & Davis 1967; Usov & Melrose 1992). We give analytic approximations for IC losses that extend into the Klein-Nishina regime and simplify the spectrum of the target photon field for Compton scattering to be monochromatic, which is suitable for strongly peaked soft photon fields like blackbodies. The present model treats the photospheric radiation field of the star closest to the collision region as the dominant target photon field for IC scattering. A minor contribution to the IC component might be expected during the onset of dust formation, which is episodically formed near periastron passage (e.g., Williams et al. 1990), from its IR radiation field that acts as an additional target photon field. This will be evaluated in a forthcoming paper. All other target radiation fields like the cosmic microwave background are negligibly small for IC photon production when compared to the dominating stellar radiation fields of the system. Furthermore, we restrict the application of our model to long-period binaries to avoid effects of radiative braking and from the radiation field and wind of the WR star for photon production processes.

Apart from any uncertainties or unknowns of the geometric parameters of the system like inclination, binary distance, size of the emission region, etc., the free parameters of our model are essentially the shock compression ratio, the diffusion coefficients, and convection velocity, which influence acceleration and propagation, the magnetic field in the colliding wind region, the winds' metallicity, and most importantly, the overall injected particle energy. Limitations from physics laws and observations were obeyed when applicable. Although many free parameters are involved in the presented model for high-energy emission from the wind collision region of massive binaries, few of them are unrelated to observations, and even fewer are those that—if altering—may have a significant impact on the predicted γ-ray intensity. Indeed, since IC emission seems to be the dominant emission process at high energies in most cases, the high-energy output can directly be deduced from the knowledge of the synchrotron emission. While the nonthermal radio flux level provides information on the required injected energy in form of electrons if the magnetic field is known, its radio spectrum constrains acceleration and propagation parameters. Equipartition arguments, together with lower magnetic field limits from the Razin-Tsytovich effect (e.g., Chen 1992; Benaglia & Romero 2003), and observational limits on the stellar surface magnetic field in connection with a plausible dipole field configuration, can be used to estimate the magnetic field strength in the collision region. The fact that relativistic electrons exist supplies a lower limit on the acceleration rate, while an upper limit is given by the Bohm diffusion regime for the likely case of diffusive shock acceleration operating in these objects.

We applied our model to two archetypal WR systems; WR 140 is arguably the more popular among these sources. We predict WR 140 to be detectable with *GLAST* and MAGIC, except at phases close to periastron due to a cutoff of the electron spectrum already at $\sim$100 MeV. This may lead to the dominance of bremsstrahlung and hadronically produced γ-rays above $\sim$1 MeV at this phase, while at phases far from periastron IC radiation is predicted to dominate at all energies. Orbital flux variations at high energies far from periastron are expected with amplitudes that vary by a factor of $\sim$2.

The 10 times more separated companions in the binary system WR 147 are notable for being the brightest (because closest) system at radio frequencies and for being one of the few systems in which the thermal and nonthermal radio emission is observed to arise from spatially different resolved regions. Due to a lack of knowledge of the system parameters, we model WR 147 face-on with no significant eccentricity. The low target photon density at the collision location makes photon absorption negligible here and at the same time allows the electron spectrum to extend up to sub-TeV energies if the acceleration efficiency is favorable. This would lead to radiation up to the 100 GeV region on a flux level possibly detectable even with VERITAS at some orbital phases, while *GLAST* has good chances to trace this system at all phases. *INTEGRAL's* sensitivity at γ-ray energies will most likely be insufficient to discover these sources as γ-ray emitters, given the finite amount of observation time in individual instrumental pointings.

Aiming toward emphasizing colliding wind binaries as potential high-energy sources, we have chosen rather optimistic parameter values for the overall injected particle energy and diffusion coefficients for both sources WR 140 and WR 147, while all other parameters are, in principle, either constrained from observations within the usual uncertainties, or plausible estimates exist (see above).

In this work we concentrated on the emission from a steady state particle spectrum. Being orbitally modulated systems in general, a time-dependent diffusion-loss equation shall give a more realistic description of the emitted intensity. In this case we expect that, similar to supernova remnants, the electron spectrum will slowly be built up, with the maximum particle energy increasing with time. Typically, the electron spectrum is fully developed after a few tens of hours. The uncertainty of a given phase corresponding to the steady state emission calculated here therefore lies in this time range. A more comprehensive discussion of the behavior of massive colliding wind systems in the framework of a time-dependent diffusion loss equation will be considered in a forthcoming paper.

In conclusion, we consider colliding wind regions of massive binary systems that are wide enough to not be affected by radiative braking as promising sources of high-energy emission that may extend far beyond the X-ray band. High-energy observations of these systems by sensitive, low-threshold IACTs and satellite experiments can be used not only to derive geometric details but also to explore the efficiency of diffusive shock acceleration at densities much higher than in other astronomical objects with high Mach number shocks.

This work was partially supported by a Lise-Meitner fellowship from the Ministerium für Wissenschaft und Forschung des Landes NRW. We also thank an anonymous referee for comments that improved this manuscript.

APPENDIX A

SOLUTIONS FOR STEADY STATE ELECTRON DISTRIBUTIONS IN THE ACCELERATION REGION

Here we derive the analytical solutions of equation (4) for electrons suffering radiative losses following equation (8). If $\Delta > 0$, then

$$N(E) = \frac{Q_0}{(a - b_{\rm br})E - b_{\rm syn\&IC}E^2 - b_{\rm coul}} \left\{ \frac{\left[H(E) - \sqrt{\Delta}\right]\left[H(E_0) + \sqrt{\Delta}\right]}{\left[H(E) + \sqrt{\Delta}\right]\left[H(E_0) - \sqrt{\Delta}\right]} \right\}^{-1/\sqrt{|\Delta|}T_0} \tag{A1}$$

for $E \le E_c = \min[(a - b_{\rm br} - \sqrt{\Delta})/2b_{\rm syn\&IC}, (a - b_{\rm br} + \sqrt{\Delta})/2b_{\rm syn\&IC}]$; with $b_{\rm syn\&IC} = b_{\rm syn} + b_{\rm IC,TL}$, $H(E) = a - b_{\rm br} - 2b_{\rm syn\&IC}E$, and $\Delta = (a - b_{\rm br})^2 - 4b_{\rm syn\&IC}b_{\rm coul}$, $N(E) = 0$ for $E > E_c$. If $\Delta \le 0$, then

$$N(E) = \frac{Q_0}{(a - b_{\rm br})E - b_{\rm syn\&IC}E^2 - b_{\rm coul}} \exp\left(-\frac{2}{T_0\sqrt{|\Delta|}} \arctan\left\{ \frac{2b_{\rm syn\&IC}(E_0 - E)\sqrt{|\Delta|}}{\left[(a - b_{\rm br}) - 2b_{\rm syn\&IC}E\right]\left[(a - b_{\rm br}) - 2b_{\rm syn\&IC}E_0\right] - \Delta} \right\} \right), \tag{A2}$$

which is an exact solution for $E < E_{\rm TL}$. With the approximation equations (9) and (10) for the IC losses, equations (A1) and (A2) describe the electron spectrum for $E > E_s$ if one substitutes $b_{\rm syn\&IC} \to b_{\rm syn}$, $b_{\rm br} \to b_{\rm br} + q_a$, and $b_{\rm coul} \to b_{\rm coul} + q_b$. In practice, however, relativistic bremsstrahlung and Coulomb losses above $E > E_{\rm TL}$ can usually be neglected in the systems considered here. For $E_{\rm TL} \le E \le E_s$ the solution of equation (4) reads

$$N(E) = \frac{Q_0}{E\left[(a - b_{\rm br}) - b_{\rm syn\&IC}E + b_{\rm IC,TL}E^2/E_g\right]} \left\{ \frac{E^2\left[(a - b_{\rm br}) - b_{\rm syn\&IC}E_0 + b_{\rm IC,TL}E_0^2/E_g\right]}{E_0^2\left[(a - b_{\rm br}) - b_{\rm syn\&IC}E + b_{\rm IC,TL}/E_gE^2\right]} \right\}^{-1/[2(a-b_{\rm br})T_0]}$$
$$\times \left[\frac{\left(2b_{\rm IC,TL}E/E_g - b_{\rm syn\&IC} - \sqrt{\Delta}\right)\left(2b_{\rm IC,TL}E_0/E_g - b_{\rm syn\&IC} + \sqrt{\Delta}\right)}{\left(2b_{\rm IC,TL}E/E_g - b_{\rm syn\&IC} + \sqrt{\Delta}\right)\left(2b_{\rm IC,TL}E_0/E_g - b_{\rm syn\&IC} - \sqrt{\Delta}\right)} \right]^{-b_{\rm syn\&IC}/\left[2T_0(a-b_{\rm br})\sqrt{\Delta}\right]}, \tag{A3}$$

for $\Delta = b_{\rm syn\&IC}^2 - 4(a - b_{\rm br})b_{\rm IC,TL}/E_g > 0$ and $N(E > E_c) = 0$, with $E < E_c = \min[(b_{\rm syn\&IC} + \sqrt{\Delta})E_g/2b_{\rm IC,TL}, (b_{\rm syn\&IC} - \sqrt{\Delta})E_g/2b_{\rm IC,TL}]$. For $\Delta < 0$ the solution is

$$N(E) = \frac{Q_0}{E\left[(a - b_{\rm br}) - b_{\rm syn\&IC}E + b_{\rm IC,TL}E^2/E_g\right]} \left\{ \frac{E^2\left[(a - b_{\rm br}) - b_{\rm syn\&IC}E_0 + b_{\rm IC,TL}E_0^2/E_g\right]}{E_0^2\left[(a - b_{\rm br}) - b_{\rm syn\&IC}E + b_{\rm IC,TL}E^2/E_g\right]} \right\}^{-1/[2(a-b_{\rm br})T_0]}$$
$$\times \exp\left\{ -\frac{b_{\rm syn\&IC}}{(a - b_{\rm br})T_0\sqrt{|\Delta|}} \arctan\left[\frac{2b_{\rm IC,TL}/E_g\sqrt{|\Delta|}(E - E_0)}{\left(2b_{\rm IC,TL}E/E_g - b_{\rm syn\&IC}\right)\left(2b_{\rm IC,TL}E_0/E_g - b_{\rm syn\&IC}\right) - \Delta} \right] \pm \pi \right\}. \tag{A4}$$

APPENDIX B

SOLUTIONS FOR STEADY STATE NUCLEON DISTRIBUTIONS IN THE ACCELERATION REGION

Here we derive analytical solutions for steady state nucleon spectra solving equation (4). At nonrelativistic energies and below the Coulomb barrier the solution is

$$N(E) = \frac{Q_0}{(a - b_{\rm bel})E} \left(\frac{E}{E_0} \right)^{-1/(a-b_{\rm bel})T_0} \tag{B1}$$

for $E < E_c$ and $N(E > E_c) = 0$, while above the Coulomb barrier $E > E_m$, we find

$$N(E) = \frac{Q_0}{aE - b_{\rm ab}E^{-0.5}} \left(\frac{E_c^{1.5} - E^{1.5}}{E_c^{1.5} - E_0^{1.5}} \right)^{-2/3aT_0} \tag{B2}$$

for $E_0 > E_m$ and $E_c = (b_{\rm ab}/a)^{2/3}$;

$$N(E) = \frac{Q_0}{aE - b_{\rm ab}E^{-0.5}} \left(\frac{E_c^{1.5} - E^{1.5}}{E_c^{1.5} - E_0^{1.5}} \right)^{-2/3aT_0} \left(\frac{E_m}{E_0} \right)^{-1/(a-b_{\rm bel})T_0} \tag{B3}$$

for $E_0 < E_m$.

At relativistic energies $>m_p c^2 = E_{\rm rel}$ and above $E > E_{\rm thr}$, the pp-interaction threshold, one finds

$$N(E) = \frac{Q_0}{(a-b_{\rm pp})E - b_{\rm rel}} \left[\frac{(a-b_{\rm pp})E - b_{\rm rel}}{(a-b_{\rm pp})E_0 - b_{\rm rel}}\right]^{-1/(a-b_{\rm pp})T_0} \left(\frac{E_m}{E_0}\right)^{-1/(a-b_{\rm bel})T_0} \left(\frac{E_c^{1.5} - E_{\rm rel}^{1.5}}{E_c^{1.5} - E_m^{1.5}}\right)^{-2/3aT_0} \left(\frac{aE_{\rm thr} - b_{\rm rel}}{aE_{\rm rel} - b_{\rm rel}}\right)^{-1/aT_0} \tag{B4}$$

for $E_0 \le E_m$,

$$N(E) = \frac{Q_0}{(a-b_{\rm pp})E - b_{\rm rel}} \left[\frac{(a-b_{\rm pp})E - b_{\rm rel}}{(a-b_{\rm pp})E_0 - b_{\rm rel}}\right]^{-1/(a-b_{\rm pp})T_0} \left(\frac{E_c^{1.5} - E_{\rm rel}^{1.5}}{E_c^{1.5} - E_0^{1.5}}\right)^{-2/3aT_0} \left(\frac{aE_{\rm thr} - b_{\rm rel}}{aE_{\rm rel} - b_{\rm rel}}\right)^{-1/aT_0} \tag{B5}$$

for $E_m < E_0 \le E_{\rm rel}$, and

$$N(E) = \frac{Q_0}{(a-b_{\rm pp})E - b_{\rm rel}} \left[\frac{(a-b_{\rm pp})E - b_{\rm rel}}{(a-b_{\rm pp})E_0 - b_{\rm rel}}\right]^{-1/(a-b_{\rm pp})T_0} \left(\frac{aE_{\rm thr} - b_{\rm rel}}{aE_0 - b_{\rm rel}}\right)^{-1/aT_0} \tag{B6}$$

for $E_{\rm rel} < E_0 \le E_{\rm thr}$.

Finally, at relativistic energies, but below $E < E_{\rm thr}$, the steady state spectrum turns out to follow

$$N(E) = \frac{Q_0}{aE - b_{\rm rel}} \left(\frac{aE - b_{\rm rel}}{aE_m - b_{\rm rel}}\right)^{-1/aT_0} \left(\frac{E_m}{E_0}\right)^{-1/(a-b_{\rm bel})T_0} \left(\frac{E_c^{1.5} - E_{\rm rel}^{1.5}}{E_c^{1.5} - E_m^{1.5}}\right)^{-2/3aT_0} \tag{B7}$$

for $E_0 \le E_m$, and

$$N(E) = \frac{Q_0}{aE - b_{\rm rel}} \left(\frac{aE - b_{\rm rel}}{aE_m - b_{\rm rel}}\right)^{-1/aT_0} \left(\frac{E_c^{1.5} - E_{\rm rel}^{1.5}}{E_c^{1.5} - E_0^{1.5}}\right)^{-2/3aT_0} \tag{B8}$$

for $E_m < E_0 \le E_{\rm rel}$.

APPENDIX C

ANALYTICAL CALCULATION OF THE INVERSE COMPTON SCATTERING RATE

In the lab frame we choose a polar coordinate system such that the line of sight marks the z-axis. A single incident electron is then fully described by its Lorentz factor, γ, and the polar angle, $\mu_e = \cos\theta_e$, and azimuthal angle, ϕ_e, to mark its direction of flight.

The photon field is described by the differential photon spectrum,

$$n_{\rm ph}(\epsilon, \Omega_{\rm ph}) = \frac{dn}{dV d\epsilon d\Omega_{\rm ph}}, \tag{C1}$$

where $\epsilon = E_{\rm ph}/m_e c^2$ is the dimensionless photon energy.

The scattering rate (quantities of the scattered photon are indexed with s) for a given differential number density of electrons, $n_e(\gamma, \Omega_e)$, is

$$\dot{n}(\epsilon_s, \Omega_s) = \oint \int d\gamma\, d\Omega_e\, n_e(\gamma, \Omega_e) \left[c \oint \int (1 - \beta\mu_{{\rm ph},e}) n_{\rm ph}(\epsilon, \Omega_{\rm ph}) \frac{d\sigma}{d\Omega_s d\epsilon_s}\, d\epsilon\, d\Omega_{\rm ph}\right], \tag{C2}$$

where the part in brackets is the scattering rate for a single electron and $\mu_{{\rm ph},e}$ is the cosine of the angle between the photon and electron flight directions, i.e.,

$$\mu_{{\rm ph},e} = \mu_e \mu_{\rm ph} + \sqrt{1-\mu_e^2}\sqrt{1-\mu_{\rm ph}^2}\cos\phi_e. \tag{C3}$$

The differential cross section is well known in the electron rest frame. It is therefore attractive to calculate the scattering rate per single electron in its rest frame (ERF, indicated by an asterisk) and then to transform the result back into the lab frame. Since then only photon spectra have to be transformed, we can use the invariants,

$$\frac{n_{\rm ph}(\epsilon, \Omega_{\rm ph})}{\epsilon^2}, \qquad \frac{\dot{n}_{\rm ph}(\epsilon, \Omega_{\rm ph})}{\epsilon}. \tag{C4}$$

C1. THE SCATTERING RATE FOR A SINGLE ELECTRON

In the following we assume that the electrons have an isotropic distribution, in which case the scattering rate cannot depend on the azimuthal angle of the incoming photons. Therefore, we can set $\phi_{\rm ph} = 0$.

The Lorentz transformation relating lab-frame quantities to those in the ERF are

$$\mu^*_{{\rm ph},e} = \frac{\mu_{{\rm ph},e} - \beta}{1 - \beta\mu_{{\rm ph},e}}, \tag{C5}$$

$$\epsilon^* = \gamma\epsilon(1 - \beta\mu_{{\rm ph},e}) = \frac{\epsilon}{\gamma(1 + \beta\mu^*_{{\rm ph},e})}. \tag{C6}$$

We also need to know the photons' azimuthal angle with respect to the electron. Let the azimuthal angle of the line of sight be $\phi_{{\rm los},e} = 0$. Then

$$\cos\phi_{{\rm ph},e} = \frac{\mu_{\rm ph}\sqrt{1-\mu_e^2} - \cos\phi_e\mu_e\sqrt{1-\mu^2_{\rm ph}}}{\sqrt{1-\mu^2_{{\rm ph},e}}}, \tag{C7}$$

$$\sin\phi_{{\rm ph},e} = \frac{\sin\phi_e\sqrt{1-\mu^2_{\rm ph}}}{\sqrt{1-\mu^2_{{\rm ph},e}}}. \tag{C8}$$

Note that $\phi_{{\rm ph},e} = \phi^*_{{\rm ph},e}$.

The differential cross section in the ERF is

$$\frac{d\sigma}{d\Omega^*_s d\epsilon^*_s} = \frac{r_e^2(1+\cos^2\xi)\delta\{\epsilon^*_s - \epsilon^*/[1+\epsilon^*(1-\cos\xi)]\}}{2[1+\epsilon^*(1-\cos\xi)]^2}\left\{1 + \frac{\epsilon^{*2}(1-\cos\xi)^2}{(1+\cos^2\xi)[1+\epsilon^*(1-\cos\xi)]}\right\}, \tag{C9}$$

where ξ is the scattering angle.

Given the photon angles after scattering, $\mu^*_{s,e}$ and $\phi^*_{s,e} = \phi_{s,e}$, the scattering angle can be calculated as

$$\cos\xi = \mu^*_{{\rm ph},e}\mu^*_{s,e} + \sqrt{1-\mu^{*2}_{{\rm ph},e}}\sqrt{1-\mu^{*2}_{s,e}}\cos(\phi_{{\rm ph},e} - \phi_{s,e}), \tag{C10}$$

where

$$\cos(\phi_{{\rm ph},e} - \phi_{s,e}) = \cos\phi_{{\rm ph},e}\cos\phi_{s,e} + \sin\phi_{{\rm ph},e}\sin\phi_{s,e}. \tag{C11}$$

Then the scattering rate in the ERF is

$$\dot{n}^*(\epsilon^*_s, \Omega^*_s) = c\int\oint\frac{\epsilon^*}{\gamma\epsilon}n_{\rm ph}(\epsilon,\Omega_{\rm ph})\frac{d\sigma}{d\epsilon^*_s d\Omega^*_s}\,d\Omega d\epsilon, \tag{C12}$$

which can be transformed back into the lab system using equation (C4) and

$$\mu_{s,e} = \frac{\mu^*_{s,e} + \beta}{1 + \beta\mu^*_{s,e}}, \tag{C13}$$

$$\epsilon_s = \epsilon^*_s\gamma(1 + \beta\mu^*_{s,e}) = \frac{\epsilon^*_s}{\gamma(1 - \beta\mu_{s,e})}. \tag{C14}$$

Finally we obtain the scattering rate in the lab frame for a population of electrons,

$$\dot{n}(\epsilon_s,\Omega_s) = \int\oint\int\oint d\epsilon\, d\Omega_{\rm ph}\, d\gamma\, d\Omega_e\,\frac{c(1-\beta\mu_{{\rm ph},e})}{\gamma(1-\beta\mu_{s,e})}n_{\rm ph}(\epsilon,\Omega_{\rm ph})n_e(\gamma,\Omega_e)\,\frac{d\sigma}{d\epsilon^*_s d\Omega^*_s}. \tag{C15}$$

C2. THE SCATTERING RATE FOR AN ARBITRARY ISOTROPIC ELECTRON SPECTRUM

Note that the line of sight is defined by $\phi_{s,e} = 0$ and $\mu_{s,e} = \mu_e$. Therefore, $\cos(\phi_{\mathrm{ph},e} - \phi_{s,e}) = \cos\phi_{\mathrm{ph},e}$. Also, $(1-\mu^{*2}) = (1-\mu^2)/\gamma^2(1-\beta\mu)^2$; hence,

$$\cos\xi = \frac{(\mu_e-\beta)(\mu_{\mathrm{ph},e}-\beta) + \gamma^{-2}\sqrt{1-\mu_e^2}\sqrt{1-\mu_{\mathrm{ph},e}^2}\cos\phi_{\mathrm{ph},e}}{(1-\beta\mu_e)(1-\beta\mu_{\mathrm{ph},e})},$$

$$= 1 - \frac{1-\mu_{\mathrm{ph}}}{\gamma^2(1-\beta\mu_e)(1-\beta\mu_{\mathrm{ph},e})}, \tag{C16}$$

$$1-\cos\xi = \frac{1-\mu_e\mu_{\mathrm{ph},e} - \sqrt{1-\mu_e^2}\sqrt{1-\mu_{\mathrm{ph},e}^2}\cos\phi_{\mathrm{ph},e}}{\gamma^2(1-\beta\mu_e)(1-\beta\mu_{\mathrm{ph},e})}, \tag{C17}$$

$$\epsilon^*(1-\cos\xi) = \epsilon\frac{1-\mu_e\mu_{\mathrm{ph},e} - \sqrt{1-\mu_e^2}\sqrt{1-\mu_{\mathrm{ph},e}^2}\cos\phi_{\mathrm{ph},e}}{\gamma(1-\beta\mu_e)} = \epsilon\frac{1-\mu_{\mathrm{ph}}}{\gamma(1-\beta\mu_e)}. \tag{C18}$$

The scattering rate does not depend on ϕ_{ph}, this integral thus being trivial. For the angles ϕ_e and μ_e, one is trivially performed by using the δ-functional in the cross section, and the other one has to be done explicitly.

The δ-functional in equation (C9) can be rewritten as

$$\delta\left(\epsilon_s - \frac{\epsilon\gamma(1-\beta\mu_{\mathrm{ph},e})}{\gamma(1-\beta\mu_e)+\epsilon\left(1-\mu_{\mathrm{ph}}\right)}\right) = \delta\Big(f(\mu_e,\mu_{\mathrm{ph}},\phi_e)\Big). \tag{C19}$$

With $n_{\mathrm{ph}}(\mu_{\mathrm{ph}}) = \int d\phi_{\mathrm{ph}}\, n_{\mathrm{ph}}(\Omega_{\mathrm{ph}})$ the scattering rate is

$$\dot{n}(\epsilon_s,\Omega_s) = \int d\epsilon \int d\mu_{\mathrm{ph}} \int d\gamma \oint d\Omega_e \frac{r_e^2 c n_e(\gamma,\Omega_e) n_{\mathrm{ph}}\left(\epsilon,\mu_{\mathrm{ph}}\right)\left(1-\beta\mu_{\mathrm{ph},e}\right)}{2\left[\gamma(1-\beta\mu_e)+\epsilon\left(1-\mu_{\mathrm{ph}}\right)\right]^2}\delta\Big(f\Big(\mu_e,\mu_{\mathrm{ph}},\phi_e\Big)\Big)$$
$$\times\left\{1+\left[1-\frac{1-\mu_{\mathrm{ph}}}{\gamma^2(1-\beta\mu_e)\left(1-\beta\mu_{\mathrm{ph},e}\right)}\right]^2 + \frac{\epsilon^2\left(1-\mu_{\mathrm{ph}}\right)^2}{\gamma(1-\beta\mu_e)\left[\gamma(1-\beta\mu_e)+\epsilon\left(1-\mu_{\mathrm{ph}}\right)\right]}\right\}. \tag{C20}$$

Given the argument f of the δ-functional,

$$\frac{\left(1-\beta\mu_{\mathrm{ph},e}\right)}{\gamma(1-\beta\mu_e)+\epsilon\left(1-\mu_{\mathrm{ph}}\right)} = \frac{\epsilon_s}{\gamma\epsilon} \tag{C21}$$

and

$$\frac{1}{\left(1-\beta\mu_{\mathrm{ph},e}\right)} = \frac{\gamma\epsilon/\epsilon_s}{\gamma(1-\beta\mu_e)+\epsilon\left(1-\mu_{\mathrm{ph}}\right)}, \tag{C22}$$

as well as

$$\delta(f) = \left[\gamma(1-\beta\mu_e)+\epsilon\left(1-\mu_{\mathrm{ph}}\right)\right]\delta\Big(g=\epsilon_s\left[\gamma(1-\beta\mu_e)+\epsilon\left(1-\mu_{\mathrm{ph}}\right)\right]-\epsilon\gamma\left(1-\beta\mu_{\mathrm{ph},e}\right)\Big). \tag{C23}$$

Using the isotropy of cosmic-ray electrons, $n_e(\gamma,\Omega_e) = n_e(\gamma)/4\pi$, we then obtain for the scattering rate,

$$\dot{n}(\epsilon_s,\Omega_s) = \frac{r_e^2 c\epsilon_s}{8\pi}\int d\epsilon \int d\mu_{\mathrm{ph}} \int d\gamma \oint d\Omega_e \frac{n_e(\gamma) n_{\mathrm{ph}}\left(\epsilon,\mu_{\mathrm{ph}}\right)}{\gamma\epsilon}\delta\Big(g\Big(\mu_e,\mu_{\mathrm{ph}},\phi_e\Big)\Big)$$
$$\times\left(1+\left\{1-\frac{\epsilon\left(1-\mu_{\mathrm{ph}}\right)}{\gamma\epsilon_s(1-\beta\mu_e)\left[\gamma(1-\beta\mu_e)+\epsilon\left(1-\mu_{\mathrm{ph}}\right)\right]}\right\}^2 + \frac{\epsilon^2\left(1-\mu_{\mathrm{ph}}\right)^2}{\gamma(1-\beta\mu_e)\left[\gamma(1-\beta\mu_e)+\epsilon\left(1-\mu_{\mathrm{ph}}\right)\right]}\right). \tag{C24}$$

Now we need to find the zeros of the δ-functional. Inserting equation (C3) into $g = 0$, we obtain

$$\epsilon_s\left[1+\frac{\epsilon}{\gamma}\left(1-\mu_{\rm ph}\right)\right]-\epsilon-\beta\left(\epsilon_s-\mu_{\rm ph}\epsilon\right)\mu_e=-\beta\epsilon\cos\phi_e\sqrt{1-\mu_{\rm ph}^2}\sqrt{1-\mu_e^2}, \tag{C25}$$

which is of the form

$$A-B\mu_e=-C\sqrt{1-\mu_e^2}, \tag{C26}$$

where C can be positive and negative, depending on ϕ_e. Also, $A > 0$ and $B > 0$ for the interesting case $\epsilon_s > \epsilon$. Real zeroes μ_0 of the above equation exist, if $B^2 + C^2 - A^2 \geq 0$.

C3. THE CASE $\mu_{\rm ph} = \pm 1$

If $\mu_{\rm ph} = \pm 1$, we have $C = 0$ and then $\mu_0 = A/B$. The δ-functional transforms as

$$\delta(g)=\frac{1}{\gamma B}\delta\left(\mu_e-\frac{A}{B}\right), \tag{C27}$$

and

$$\dot{n}(\epsilon_s,\Omega_s)\Big|_{\mu_{\rm ph}=\pm1}=\frac{r_e^2c\epsilon_s}{4}\int d\epsilon\int d\gamma\,\frac{n_e(\gamma)n_{\rm ph}\left(\epsilon,\mu_{\rm ph}=\pm1\right)}{\gamma^2\epsilon B}\Theta(B-A)$$
$$\times\left(1+\left\{1-\frac{\epsilon\left(1-\mu_{\rm ph}\right)}{\gamma\epsilon_s(1-\beta\mu_0)\left[\gamma(1-\beta\mu_0)+\epsilon\left(1-\mu_{\rm ph}\right)\right]}\right\}^2+\frac{\epsilon^2\left(1-\mu_{\rm ph}\right)^2}{\gamma(1-\beta\mu_0)\left[\gamma(1-\beta\mu_0)+\epsilon\left(1-\mu_{\rm ph}\right)\right]}\right). \tag{C28}$$

C3.1. $\mu_{\rm ph} = +1$

Here obviously $B/A = \beta < 1$, which implies that the argument of the δ-functional, g, has no zero in the range of integration, and thus the scattering rate in the forward direction is precisely zero.

C3.2. $\mu_{\rm ph} = -1$

Here

$$B=\beta(\epsilon_s+\epsilon),\qquad A=\epsilon_s\left(1+\frac{2\epsilon}{\gamma}\right)-\epsilon, \tag{C29}$$

and then

$$\mu_e=\frac{A}{B}\leq1\Rightarrow\epsilon_s\leq\left(\frac{1+\beta}{2\epsilon/\gamma+1-\beta}\right)\epsilon. \tag{C30}$$

Then also

$$1-\beta\mu_0=\frac{2\epsilon}{\gamma}\frac{\gamma-\epsilon_s}{\epsilon_s+\epsilon}, \tag{C31}$$

and

$$\gamma(1-\beta\mu_0)\left[\gamma(1-\beta\mu_0)+\epsilon\left(1-\mu_{\rm ph}\right)\right]=\frac{4\epsilon^2}{(\epsilon_s+\epsilon)^2}\left[\gamma^2-(\epsilon_s-\epsilon)\gamma-\epsilon\epsilon_s\right]. \tag{C32}$$

Therefore,

$$\dot{n}(\epsilon_s,\Omega_s)\Big|_{\mu_{\rm ph}=-1}=\frac{r_e^2c\epsilon_s}{4}\int d\epsilon\int d\gamma\,\frac{n_e(\gamma)n_{\rm ph}\left(\epsilon,\mu_{\rm ph}=-1\right)}{\beta\gamma^2\epsilon(\epsilon_s+\epsilon)}\Theta\left(\left(\frac{1+\beta}{2\epsilon/\gamma+1-\beta}\right)-\epsilon_s\right)$$
$$\times\left(1+\left\{1-\frac{(\epsilon_s+\epsilon)^2}{2\epsilon\epsilon_s[\gamma^2-(\epsilon_s-\epsilon)\gamma-\epsilon\epsilon_s]}\right\}^2+\frac{(\epsilon+\epsilon_s)^2}{[\gamma^2-(\epsilon_s-\epsilon)\gamma-\epsilon\epsilon_s]}\right), \tag{C33}$$

where Θ denotes a step function.

C4. THE CASE $\mu_{\rm ph} \neq \pm 1$

We obtain formally by squaring equation (C26),

$$\mu_e = \frac{AB \pm |C|\sqrt{B^2 + C^2 - A^2}}{B^2 + C^2}.$$

Since we have squared the original equation, not all formal solutions may apply. The ambiguity in sign is combined with the modulus of C; therefore, writing C instead of $|C|$ does not introduce new solutions. Then, assuming $A > 0$ and $B > 0$, i.e., up-scattering of photons in energy, we find

$$\mu_e = \frac{AB \pm C\sqrt{B^2 + C^2 - A^2}}{B^2 + C^2} \tag{C34}$$

is a solution to the original equation,

$$\text{case } \oplus \text{ if } C \leq \frac{B}{A}\sqrt{B^2 + C^2 - A^2}, \tag{C35}$$

$$\text{case } \ominus \text{ if } C \leq -\frac{B}{A}\sqrt{B^2 + C^2 - A^2}. \tag{C36}$$

The δ-functional in equation (C24) transforms as

$$\delta(g) = \frac{B\mu_e - A}{\gamma C\sqrt{B^2 + C^2 - A^2}}\,\delta(\mu_e - \mu_0). \tag{C37}$$

Then

$$\dot{n}(\epsilon_s, \Omega_s) = \frac{r_e^2 c \epsilon_s}{4\pi}\int d\epsilon \int d\mu_{\rm ph} \int d\gamma \int_0^{\pi} d\phi_e \, \frac{n_e(\gamma) n_{\rm ph}\left(\epsilon, \mu_{\rm ph}\right)}{\gamma^2 \epsilon} \frac{\Theta(B^2 + C^2 - A^2)}{C\sqrt{B^2 + C^2 - A^2}} \sum_{\pm} (B\mu_0 - A)\Theta\left(\pm\frac{B}{A}\sqrt{B^2 + C^2 - A^2} - C\right)$$
$$\times \left(1 + \left\{1 - \frac{\epsilon\left(1 - \mu_{\rm ph}\right)}{\gamma\epsilon_s(1 - \beta\mu_0)\left[\gamma(1 - \beta\mu_0) + \epsilon\left(1 - \mu_{\rm ph}\right)\right]}\right\}^2 + \frac{\epsilon^2\left(1 - \mu_{\rm ph}\right)^2}{\gamma(1 - \beta\mu_0)\left[\gamma(1 - \beta\mu_0) + \epsilon\left(1 - \mu_{\rm ph}\right)\right]}\right). \tag{C38}$$

The integration variable ϕ_e appears only as the argument of a cosine function, which itself appears only in the term C. We can therefore substitute C for ϕ_e. With $C_1 = \beta\epsilon(1 - \mu_{\rm ph}^2)^{1/2}$,

$$\int_0^{\pi} d\phi_e = \int_{-C_1}^{C_1} \frac{dC}{\sqrt{C_1^2 - C^2}}, \tag{C39}$$

and we obtain

$$\dot{n}(\epsilon_s, \Omega_s) = \frac{r_e^2 c \epsilon_s}{4\pi}\int d\epsilon \int d\mu_{\rm ph} \int d\gamma \int_{-C_1}^{C_1} dC \, \frac{n_e(\gamma) n_{\rm ph}\left(\epsilon, \mu_{\rm ph}\right)}{\gamma^2 \epsilon C\sqrt{C_1^2 - C^2}} \frac{\Theta(B^2 + C^2 - A^2)}{\sqrt{B^2 + C^2 - A^2}} \sum_{\pm} (B\mu_0 - A)\Theta\left(\pm\frac{B}{A}\sqrt{B^2 + C^2 - A^2} - C\right)$$
$$\times \left(1 + \left\{1 - \frac{\epsilon\left(1 - \mu_{\rm ph}\right)}{\gamma\epsilon_s(1 - \beta\mu_0)\left[\gamma(1 - \beta\mu_0) + \epsilon\left(1 - \mu_{\rm ph}\right)\right]}\right\}^2 + \frac{\epsilon^2\left(1 - \mu_{\rm ph}\right)^2}{\gamma(1 - \beta\mu_0)\left[\gamma(1 - \beta\mu_0) + \epsilon\left(1 - \mu_{\rm ph}\right)\right]}\right). \tag{C40}$$

It is now useful to discriminate two cases. The first case is

$$B \geq A \Rightarrow \epsilon_s \leq \epsilon\frac{1 - \beta\mu_{\rm ph}}{1 - \beta + (\epsilon/\gamma)\left(1 - \mu_{\rm ph}\right)} = \frac{\gamma^2\epsilon(1 + \beta)\left(1 - \beta\mu_{\rm ph}\right)}{1 + \gamma\epsilon(1 + \beta)\left(1 - \mu_{\rm ph}\right)} = \epsilon_{s1}, \tag{C41}$$

for which only the $\oplus$ solution exists for all C. The second case is

$$B < A \text{ and } C_1^2 \geq A^2 - B^2 \Rightarrow \epsilon_{s1} < \epsilon_s \text{ and } \epsilon_s \leq \epsilon_{s2}, \tag{C42}$$

with

$$\epsilon_{s2} = \frac{\epsilon\gamma\left[\gamma\left(1-\beta\mu_{\rm ph}\right)+\epsilon\left(1-\mu_{\rm ph}\right)\right]}{1+2\epsilon\gamma\left(1-\mu_{\rm ph}\right)+\epsilon^2\left(1-\mu_{\rm ph}\right)^2}\left\{1+\sqrt{1-\frac{1+2\epsilon\gamma\left(1-\mu_{\rm ph}\right)+\epsilon^2\left(1-\mu_{\rm ph}\right)^2}{\left[\gamma^2\left(1-\beta\mu_{\rm ph}\right)+\epsilon\gamma\left(1-\mu_{\rm ph}\right)\right]^2}}\right\}, \tag{C43}$$

for which both the $\oplus$ and the $\ominus$ solutions exist, but only for negative $C \leq -C_2 = -(A^2 - B^2)^{1/2}$. If $\mu_{\rm ph}$ is not very close to 1, ϵ_{s2} does in fact exceed ϵ_{s2}, but only by a very small margin. The relative difference $(\epsilon_{s2} - \epsilon_{s1})/\epsilon_{s1} < 10^{-2}$ for $\gamma = 10$, and it decreases rapidly with increasing γ.

C4.1. *The Case $B \geq A$*

The integration variable C is an argument of μ_0. We may substitute $\mu = \mu_0$ for C and use

$$\int_{-C_1}^{C_1} dC\,\frac{B\mu_0 - A}{C\sqrt{C_1^2 - C^2}\sqrt{B^2 + C^2 - A^2}} = \frac{1}{\sqrt{B^2 + C_1^2}}\int_{\mu_-}^{\mu_+} d\mu\,\frac{1}{\sqrt{(\mu-\mu_-)(\mu_+-\mu)}}, \tag{C44}$$

with

$$\mu_\pm = \frac{AB \pm C_1\sqrt{B^2 + C_1^2 - A^2}}{B^2 + C_1^2}, \tag{C45}$$

to obtain the scattering rate as

$$\dot{n} = \frac{r_e^2 c\epsilon_s}{4\pi}\int d\epsilon \int d\mu_{\rm ph}\int d\gamma\,\frac{n_e(\gamma)n_{\rm ph}\left(\epsilon,\mu_{\rm ph}\right)}{\beta\gamma^2\epsilon\sqrt{\epsilon_s^2 - 2\mu_{\rm ph}\epsilon\epsilon_s + \epsilon^2}}\Theta(B-A)\int_{\mu_-}^{\mu_+}\frac{d\mu}{\sqrt{(\mu-\mu_-)(\mu_+-\mu)}}$$
$$\times\left(1+\left\{1-\frac{\epsilon\left(1-\mu_{\rm ph}\right)}{\gamma\epsilon_s(1-\beta\mu)\left[\gamma(1-\beta\mu)+\epsilon\left(1-\mu_{\rm ph}\right)\right]}\right\}^2+\frac{\epsilon^2\left(1-\mu_{\rm ph}\right)^2}{\gamma(1-\beta\mu)\left[\gamma(1-\beta\mu)+\epsilon\left(1-\mu_{\rm ph}\right)\right]}\right),$$

or

$$\dot{n}(\epsilon_s,\Omega_s) = \frac{r_e^2 c\epsilon_s}{4\pi}\int d\epsilon \int d\mu_{\rm ph}\int d\gamma\,\frac{n_e(\gamma)n_{\rm ph}(\epsilon,\mu_{\rm ph})}{\beta\gamma^2\epsilon\sqrt{\epsilon_s^2 - 2\mu_{\rm ph}\epsilon\epsilon_s + \epsilon^2}}\Theta(B-A)\int_{\mu_-}^{\mu_+}\frac{d\mu}{\sqrt{(\mu-\mu_-)(\mu_+-\mu)}}$$
$$\times\left(2+\frac{\epsilon^2\epsilon_s\left(1-\mu_{\rm ph}\right)^2-2\epsilon\left(1-\mu_{\rm ph}\right)}{\gamma\epsilon_s(1-\beta\mu)\left[\gamma(1-\beta\mu)+\epsilon\left(1-\mu_{\rm ph}\right)\right]}+\frac{\epsilon^2\left(1-\mu_{\rm ph}\right)^2}{\epsilon_s^2\left\{\gamma(1-\beta\mu)\left[\gamma(1-\beta\mu)+\epsilon\left(1-\mu_{\rm ph}\right)\right]\right\}^2}\right), \tag{C46}$$

which is essentially the sum of three integrals I_1, I_2, and I_3, which are defined by the terms in the large parentheses.

For the first integral note that

$$\int_{\mu_-}^{\mu_+}\frac{d\mu}{\sqrt{(\mu-\mu_-)(\mu_+-\mu)}} = -\arcsin\left(\frac{\mu_+ + \mu_- - 2\mu}{\mu_+ - \mu_-}\right)\Bigg|_{\mu_-}^{\mu_+} = \pi \Rightarrow I_1 = 2\pi. \tag{C47}$$

The second integral has the structure

$$I_2 = D\int_{\mu_-}^{\mu_+}\frac{d\mu}{\sqrt{(\mu-\mu_-)(\mu_+-\mu)}}\frac{1}{(\mu+a)(\mu+b)}, \tag{C48}$$

where

$$D = \frac{\epsilon(1-\mu_{\rm ph})}{\gamma^2\beta^2\epsilon_s}\Big[\epsilon\epsilon_s(1-\mu_{\rm ph})-2\Big], \qquad a = -\frac{1}{\beta}, \qquad b = -\frac{1}{\beta} - \frac{\epsilon(1-\mu_{\rm ph})}{\gamma\beta}. \tag{C49}$$

We have

$$I_2 = D\frac{\gamma\beta}{\epsilon\Big(1-\mu_{\rm ph}\Big)}\left[\int_{\mu_-}^{\mu_+}\frac{d\mu}{\sqrt{(\mu-\mu_-)(\mu_+-\mu)}}\frac{1}{(\mu+b)} - \int_{\mu_-}^{\mu_+}\frac{d\mu}{\sqrt{(\mu-\mu_-)(\mu_+-\mu)}}\frac{1}{(\mu+a)}\right] \tag{C50}$$

$$\Rightarrow I_2 = -D\frac{\gamma\beta}{\epsilon\Big(1-\mu_{\rm ph}\Big)}\left[\int_{1/\mu_-+a}^{1/\mu_++a}\frac{dt}{\sqrt{A+B_at+C_at^2}} - \int_{1/\mu_-+b}^{1/\mu_++b}\frac{dt}{\sqrt{A+B_bt+C_bt^2}}\right], \tag{C51}$$

where with (a, b) standing for a or b,

$$A_a = -1, \qquad B_{a,b} = \mu_+ + \mu_- + 2(a,b), \tag{C52}$$

$$C_{a,b} = -\mu_-\mu_+ - \big(\mu_- + \mu_+\big)(a,b) - (a,b)^2. \tag{C53}$$

Because

$$C_{a,b} < 0 \text{ and } \Delta = 4A_aC_{a,b} - B_{a,b}^2 < 0, \tag{C54}$$

the solution of the integrals in equation (C51) is

$$\int_{1/\mu_-+(a,b)}^{1/\mu_++(a,b)}\frac{dt}{\sqrt{A_a+B_{a,b}t+C_{a,b}t^2}} = -\frac{\pi}{\sqrt{-C_{a,b}}}; \tag{C55}$$

hence,

$$I_2 = -\pi\frac{\epsilon\epsilon_s\Big(1-\mu_{\rm ph}\Big)-2}{\gamma\beta\epsilon_s}\left[\frac{1}{\sqrt{\big(\mu_++b\big)\big(\mu_-+b\big)}} - \frac{1}{\sqrt{\big(\mu_++a\big)\big(\mu_-+a\big)}}\right]. \tag{C56}$$

The third integral is of the form

$$I_3 = D\int_{\mu_-}^{\mu_+}\frac{d\mu}{\sqrt{(\mu-\mu_-)(\mu_+-\mu)}}\frac{1}{(\mu+a)^2(\mu+b)^2}, \tag{C57}$$

where

$$D = \frac{\epsilon^2\Big(1-\mu_{\rm ph}\Big)^2}{\epsilon_s^2\gamma^4\beta^4}. \tag{C58}$$

We may write

$$\frac{1}{(\mu+a)^2(\mu+b)^2} = \frac{1}{(a-b)^2}\left(\frac{1}{\mu+b}-\frac{1}{\mu+a}\right)^2 = \frac{1}{(a-b)^2}\left[\frac{1}{(\mu+b)^2}+\frac{1}{(\mu+a)^2}-\frac{2}{(\mu+a)(\mu+b)}\right], \tag{C59}$$

so that

$$I_3 = \frac{1}{\epsilon_s^2\gamma^2\beta^2}\int_{\mu_-}^{\mu_+}\frac{d\mu}{\sqrt{(\mu-\mu_-)(\mu_+-\mu)}}\left[\frac{1}{(\mu+b)^2}+\frac{1}{(\mu+a)^2}-\frac{2}{(\mu+a)(\mu+b)}\right] = J_1 + J_2 + J_3. \tag{C60}$$

The integral J_3 is formally identical to I_2,

$$J_3 = \frac{2\pi}{\gamma\beta\epsilon_s^2\epsilon\Big(1-\mu_{\rm ph}\Big)}\left[\frac{1}{\sqrt{\big(\mu_++b\big)\big(\mu_-+b\big)}} - \frac{1}{\sqrt{\big(\mu_++a\big)\big(\mu_-+a\big)}}\right]. \tag{C61}$$

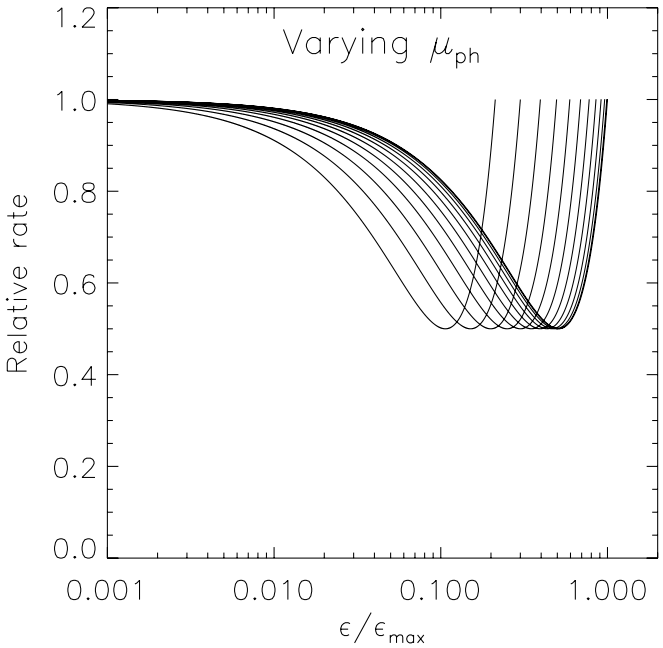

FIG. 26.—Scattering rate for $\epsilon = 10^{-7}$, $\gamma = 10^5$, and varying μ_{ph}. For curve i, the scattering angle is $\pi - 0.2i$.

The other integrals are (for J_1 replace a by b)

$$\epsilon_s^2\gamma^2\beta^2 J_2 = -\frac{\pi}{2}\frac{\mu_+ + \mu_- + 2(a,b)}{\left\{\left[\mu_+ + (a,b)\right]\left[\mu_- + (a,b)\right]\right\}^{3/2}}. \tag{C62}$$

The total scattering rate is then

$$\begin{aligned}\dot{n}(\epsilon_s,\Omega_s) = \frac{r_e^2 c\epsilon_s}{2}\int d\epsilon \int d\mu_{ph}\int d\gamma\,\frac{n_e(\gamma)n_{ph}\left(\epsilon,\mu_{ph}\right)}{\beta\gamma^2\epsilon\sqrt{\epsilon_s^2 - 2\mu_{ph}\epsilon\epsilon_s + \epsilon^2}}\Theta(\epsilon_{s1}-\epsilon_s)\\ \times\left\{1 - \frac{1}{4\epsilon_s^2\gamma^2\beta^2}\left[\frac{\mu_+ + \mu_- + 2b}{\sqrt{(\mu_+ + b)(\mu_- + b)^3}} + \frac{\mu_+ + \mu_- + 2a}{\sqrt{(\mu_+ + a)(\mu_- + a)^3}}\right]\right.\\ \left. - \left[\frac{\epsilon(1-\mu_{ph})}{2\gamma\beta} - \frac{\epsilon_s\epsilon(1-\mu_{ph})+1}{\gamma\beta\epsilon_s^2\epsilon(1-\mu_{ph})}\right]\left[\frac{1}{\sqrt{(\mu_+ + b)(\mu_- + b)}} - \frac{1}{\sqrt{(\mu_+ + a)(\mu_- + a)}}\right]\right\}.\end{aligned} \tag{C63}$$

Its spectral dependence on μ_{ph} is shown in Figure 26. Note that $(\mu_+ - \mu_-)/\mu_+$ is an extremely small number, as well as the difference of the parameters a and b. For $\mu_{ph} = -1$, we reproduce the earlier solution (C33).

REFERENCES

Abbott, D. C., Bieging, J. H., Churchwell, E., & Torres, A. V. 1986, ApJ, 303, 239
Aharonian, F., et al. 2005a, A&A, 442, 1
———. 2005b, Science, 309, 746
Barlow, M. J. 1982, in IAU Symp. 99, Wolf-Rayet Stars: Observations, Physics, Evolution (Dordrecht: Reidel), 149
Barker, P. 1986, in ASP Conf. Ser. 98, Workshop on the Connection between Nonradial Pulsations and Stellar Winds in Massive Stars (San Francisco: ASP), 44
Bell, A. R., & Lucek, S. G. 2001, MNRAS, 321, 433
Benaglia, P., & Romero, G. E. 2003, A&A, 399, 1121
Blumenthal, G. R., & Gould, R. J. 1970, Rev. Mod. Phys., 42, 237
Brunetti, G. 2000, Astropart. Phys., 13, 107
Cassé, M., & Paul, J. A. 1980, ApJ, 237, 236
Cassinelli, J. P. 1979, ARA&A, 17, 275
Chen, W. 1992, Ph.D. thesis, Johns Hopkins Univ.
Chen, W., & White, R. L. 1991, ApJ, 366, 512
Churchwell, E. B., et al. 1992, ApJ, 393, 329
Conti, P. S., & Ebbets, D. 1977, ApJ, 213, 438
Contreras, M. E., et al. 1997, ApJ, 488, L153
Dermer, C. D., & Schlickeiser, R. 1991, A&A, 252, 414
Donati, J.-F., et al. 2002, MNRAS, 333, 55
Dougherty, S. M., Williams, P. M., & Pallaco, D. L. 2000, MNRAS, 316, 143
Dougherty, S. M., et al. 1996, MNRAS, 280, 963
———. 2003, A&A, 409, 217
———. 2005, ApJ, 623, 447
Eichler, D., & Usov, V. 1993, ApJ, 402, 271
Gayley, K. G., Owocki, S. P., & Cranmer, S. R. 1997, ApJ, 475, 786
Gould, R. J., & Schreder, G. P. 1967, Phys. Rev., 155, 1404
Hartman, R. C., et al. 1999, ApJS, 123, 79
Ignace, R., Cassinelli, J. P., & Bjorkman, J. E. 1998, ApJ, 505, 910
Kaul, R. K., & Mitra, A. K. 1997, in AIP Conf. Proc. 410, Proc. Fourth Compton Symp., ed. C. D. Dermer, M. S. Strickman, & J. D. Kurfess (New York: AIP), 1271
Kirk, J. G., Ball, L., & Skjaeraasen, O. 1999, Astropart. Phys., 10, 31
Lamers, H. J. G. L. M., & Casinelli, J. P. 1999, Introduction to Stellar Winds (Cambridge: Cambridge Univ. Press)
Lucek, S. G., & Bell, A. R. 2000, MNRAS, 314, 65

Lucy, L. B., & White, R. L. 1980, ApJ, 241, 300
Luo, D., McCray, R., & Mac Low, M.-M. 1990, ApJ, 362, 267
Malkov, M. A., & Völk, H. J. 1995, A&A, 300, 605
Marchenko, S. V., et al. 2003, ApJ, 596, 1295
Mastichiadis, A. 1991, MNRAS, 253, 235
Mathys, G. 1999, in IAU Colloq. 169, Variable and Nonspherical Stellar Winds in Luminous Hot Stars, ed. B. Wolf, O. Stahl, & A. W. Fullerton (Berlin: Springer), 95
Moderski, R., Sikora, M., Coppi, P. S., & Aharonian, F. 2005, MNRAS, 363, 954
Moffat, A. F. J. 1996, in Wolf-Rayet Stars in the Framework of Stellar Evolution, ed. J. M. Vreux et al. (Liège: Univ. Liège), 199
Montmerle, T. 1979, ApJ, 231, 95
Mücke, A., & Pohl, M. 2002, in ASP Conf. Ser. 260, Interacting Winds from Massive Stars, ed. A. F. J. Moffat & N. St.-Louis (San Francisco: ASP), 355
Nolan, P. L., et al. 2003, ApJ, 597, 615
Paczynski, B. 1998, ApJ, 494, L45
Panov, K. P., Altmann, M., & Seggewiss, W. 2000, A&A, 355, 607
Penny, L. R. 1996, ApJ, 463, 737
Pfrommer, C., & Ensslin, T. A. 2004, A&A, 413, 17
Pittard, J. M., et al. 2002, A&A, 388, 335
———. 2006, A&A, 446, 1001
Pollock, A. M. T. 1987, A&A, 171, 135
Protheroe, R. J., & Stanev, T. 1999, Astropart. Phys., 10, 185
Rauw, G., et al. 2002, A&A, 394, 993
Reynolds, S. P. 1982, ApJ, 256, 38
Romero, G. E., Benaglia, P., & Torres, D. F. 1999, A&A, 348, 868
Schild, H., et al. 2004, A&A, 422, 177
Schlickeiser, R. 2002, Cosmic Ray Astrophysics (Berlin: Springer)
Setia Gunawan, D. Y. A., et al. 2001a, A&A, 368, 484
———. 2001b, A&A, 376, 460
Stevens, I. R., Blondin, J. M., & Pollock, A. M. T. 1992, ApJ, 386, 265
Stevens, I. R., & Pollock, A. M. T. 1994, MNRAS, 269, 226
Tavani, M., & Arons, J. 1997, ApJ, 477, 439
Usov, V. V. 1992, ApJ, 389, 635
Usov, V. V., & Melrose, D. B. 1992, ApJ, 395, 575
Völk, H. J., & Forman, M. 1982, ApJ, 253, 188
Weber, E. J., & Davis, L., Jr. 1967, ApJ, 148, 217
Weekes, T. C., et al. 2002, Astropart. Phys., 17, 221
White, R. L. 1985, ApJ, 289, 698
White, R. L., & Becker, R. H. 1995, ApJ, 451, 352
White, R. L., & Chen, W. 1992, ApJ, 387, L81
Williams, P. M., et al. 1990, MNRAS, 243, 662
———. 1997, MNRAS, 289, 10
Woosley, S. 1993, ApJ, 405, 273